CENTER FOR RESEARCH AND ADVANCED STUDIES OF
THE NATIONAL POLYTECHNIC INSTITUTE

Influence of co-doping on the structure and ionic conductivity of the garnet-type solid electrolyte $Li_7La_3Zr_2O_{12}$ for lithium-ion batteries

THESIS

Presented by

VERONICA ALEJANDRA DEAQUINO GARCIA

To obtain the degree of

MASTER

IN

NATURAL RESOURCES AND ENERGY SUSTAINABILITY

Thesis advisors:

Dr. Padmasree Karinjilottu Padmadas

Dr. María de Lourdes Virginia Díaz Jiménez

Ramos Arizpe, Coahuila December, 2024

CENTRO DE INVESTIGACIÓN Y DE ESTUDIOS AVANZADOS
DEL INSTITUTO POLITÉCNICO NACIONAL

UNIDAD SALTILLO

Influencia del co-dopado en la estructura y conductividad iónica del electrolito sólido tipo granate $Li_7La_3Zr_2O_{12}$ para baterías de iones de litio

TESIS

Que presenta

VERONICA ALEJANDRA DEAQUINO GARCIA

Para obtener el grado de

MAESTRÍA

EN

SUSTENTABILIDAD DE LOS RECURSOS NATURALES Y ENERGÍA

Directores de tesis:

Dr. Padmasree Karinjilottu Padmadas

Dr. María de Lourdes Virginia Díaz Jiménez

Ramos Arizpe, Coahuila

Diciembre, 2024

DEDICATION

To my dear family,

For your unconditional support in every step of this journey. Thank you for being by my side in those moments when doubts seemed to overcome me, and I felt that I could no longer continue. You have been my driving force, reminding me that difficult moments can always be overcome when you have the right people and never stop trying.

To you, who celebrated with me every achievement, every breakthrough, every happy moment, and who were present in every smile and every tear. This thesis would not have been possible without your love, your patience and your trust in me.

ACKNOWLEDGMENTS

To my parents, Claudia Verónica García López and Rogelio Deaquino Lara, for being my constant inspiration and providing me with their invaluable support and knowledge throughout my academic process. There are not enough words to express my gratitude for all your teachings and contributions. Thank you immensely.

To my brother, David Alejandro Deaquino García, who although he sometimes denies it, is always there when I need him. His presence and knowledge have been a great support for me.

To my thesis directors, Dra. María Lourdes Virginia Díaz Jiménez, for her guidance and shared experience, as well as her valuable comments, and to Dra. Padmasree Karinjilottu Padmadas, who gave me immense support, effort and knowledge during these two years of my master's degree. I have no words to thank you for having found in you such a generous and wise guide; I feel deeply honored to be your student.

To my partner, Jorge Iván García Leyva, whose experience has been crucial in guiding me in my decisions. Thank you for your willingness to always help me and for being a great moral support in the most difficult moments.

To my lab mates, Fernando, Gisela and Yair, who have made my days at the institution more comfortable, always sharing their knowledge and advice, which have helped me so much.

To Hirepan Chávez Cárdenas, who at the beginning of this process provided me with key knowledge as a basis for the development of my project and was always willing to answer my questions. Thank you very much for sharing your experience with me.

To all the workers at CINVESTAV, for their support and collaboration in carrying out the tests necessary for the development of this thesis.

Finally, I thank CONAHCyT for the scholarship that made it possible for me to complete my master's degree.

ABSTRACT

In the last decades, lithium-ion batteries (LIBs) have dominated the market in terms of mobile power sources. Commercial LIBs use organic liquid electrolytes, however, they present problems that can lead to safety risks, such as corrosion, leakage, and the possibility of exploding due to the flammability of the organic compounds in liquid electrolytes. The use of solid electrolytes made of conductive solid lithium-ion materials is an alternative with great potential for the next generations of LIBs. Among the different ceramic materials focused on solid electrolytes, $Li_7La_3Zr_2O_{12}$ (LLZO) based garnet-type have stood out for being good ionic conductors at room temperature (above 10^{-4} S cm^{-1}) and having stability towards lithium metal when acting as an anode material. However, the cubic phase of LLZO (c-LLZO) is difficult to synthesize and is not stable at room temperature. Partial substitution or doping is considered an effective way to stabilize the cubic structure and improve the lithium-ion conductivity of the material by creating vacancies and disorder in the lithium sublattice. In this work, doped and co-doped solid electrolytes were synthesized by the Pechini method. The experiment was divided into two stages. In the first stage, Li^+ sites were partially substituted by Ga^{3+} generating a series of $Li_{7-3x}Ga_xLa_3Zr_2O_{12}$ (x = 0, 0.1, 0.2 and 0.3). Subsequently, from the material with the best result in ionic conductivity, a second series was prepared, partially replacing Zr^{4+} by Gd^{3+} and obtaining the series of $Li_{7-3x+y}Ga_xLa_3Zr_{2-y}Gd_yO_{12}$ (y = 0.2, 0.4, 0.6 and 0.8). X-ray diffraction analysis of the Ga-doped series confirmed that for the samples with x = 0.2 and 0.3, it was possible to stabilize the cubic phase at room temperature with a low calcination temperature (875 °C). However, for the samples with x = 0 and 0.1, the cubic phase was obtained only after sintering at 1100 °C. This demonstrates the stabilizing effect of Ga-doping to obtain the c-LLZO structure at low temperature. For the co-doped samples, only y = 0.2 showed a pure cubic phase after sintering at 1100 °C. Among the Ga-doped samples studied, $Li_{6.4}Ga_{0.2}La_3Zr_2O_{12}$ presented the highest ionic conductivity of 1.58×10^{-04} S cm^{-1} at room temperature. From the co-doped samples, $Li_{6.6}$ $Ga_{0.2}La_3Zr_{1.8}Gd_{0.2}O_{12}$ showed the highest ionic conductivity of 2.31×10^{-04} S cm^{-1} at room temperature, being twice as high as that presented by the 0.2 Ga doped sample. Therefore, $Li_{6.6}Ga_{0.2}La_3Zr_{1.8}Gd_{0.2}O_{12}$ can be considered as a possible candidate as solid electrolyte for lithium-ion batteries (LIBs) applications.

RESUMEN

En las últimas décadas, las baterías de iones de litio (LIBs) han dominado el mercado de las fuentes de energía móviles. Las LIB comerciales utilizan electrolitos líquidos orgánicos; sin embargo, presentan problemas que pueden plantear riesgos de seguridad, como la corrosión, las fugas y la posibilidad de explosión debido a la inflamabilidad de los compuestos orgánicos dentro de los electrolitos líquidos. El uso de electrolitos sólidos hechos de materiales conductores de iones de litio es una alternativa con gran potencial para las próximas generaciones de LIBs. Entre los diferentes materiales cerámicos enfocados a electrolitos sólidos, los materiales de tipo granate basados en $Li_7La_3Zr_2O_{12}$ (LLZO) han destacado por ser buenos conductores de iones a temperatura ambiente (por encima de 10^{-4} S cm^{-1}) y tener estabilidad frente al litio metálico cuando actúan como material anódico. Sin embargo, la fase cúbica del LLZO (c-LLZO) es difícil de sintetizar y no es estable a temperatura ambiente. El dopaje se considera una forma eficaz de estabilizar la estructura cúbica y mejorar la conductividad de iones de litio del material mediante la creación de vacancias y desorden en la subred de litio.

En este trabajo se sintetizaron electrolitos sólidos co-dopados por el método Pechini. El experimento se dividió en dos etapas. En la primera etapa, los sitios Li^+ fueron parcialmente sustituidos por Ga^{3+} generando una serie de $Li_{7-3x}Ga_xLa_3Zr_2O_{12}$ (x = 0, 0.1, 0.2 y 0.3). Posteriormente, a partir del material con mejor resultado en conductividad iónica, se preparó una segunda serie, sustituyendo parcialmente Zr^{4+} por Gd^{3+} y obteniendo la serie $Li_{7-3x+y}Ga_xLa_3Zr_{2-y}Gd_yO_{12}$ (y = 0.2, 0.4, 0.6 y 0.8). El análisis de difracción de rayos X de la serie dopada con Ga confirmó que, para las muestras con x = 0.2 y 0.3, era posible estabilizar la fase cúbica a temperatura ambiente con una baja temperatura de calcinación (875 °C). Sin embargo, para las muestras con x = 0 y 0.1, la fase cúbica sólo se obtiene tras la sinterización a 1100 °C. Esto demuestra el efecto estabilizador del dopaje con Ga para obtener la estructura c-LLZO a baja temperatura. En el caso de las muestras co-dopadas, sólo y = 0.2 mostró una fase cúbica pura tras la sinterización a 1100 °C. Entre las muestras dopadas con Ga estudiadas, $Li_{6.4}Ga_{0.2}La_3Zr_2O_{12}$ presentó la conductividad iónica más elevada, de 1.58×10^{-04} S cm^{-1} a temperatura ambiente. Mientras que, de las muestras co-dopadas, $Li_{6.6}Ga_{0.2}La_3Zr_{1.8}Gd_{0.2}O_{12}$ presentó la conductividad iónica más alta, de 2.31×10^{-04} S cm^{-1} a

temperatura ambiente, siendo el doble que la presentada por la dopada con 0.2 de Ga. Por lo tanto, $Li_{6.6}\,Ga_{0.2}La_{3}Zr_{1.8}Gd_{0.2}O_{12}$ puede considerarse un posible candidato como electrolito sólido para aplicaciones en baterías de ion-litio (LIBs).

TABLE OF CONTENTS

INDEX OF FIGURES

INDEX OF TABLES

ACRONYMS

c-LLZO	Cubic phase of $Li_7La_3Zr_2O_{12}$
EV	Electric vehicles
GHG	Greenhouse gas
LATP	$Li_{1.7}Al_{0.3}Ti_{1.7}(PO4)_3$
LIBs	Lithium-ion batteries
LLZO	$Li_7La_3Zr_2O_{12}$
SSB	Solid-state batteries
SSLIBs	Solid-state lithium-ion batteries
SEs	Solid electrolytes
t-LLZO	Tetragonal phase of $Li_7La_3Zr_2O_{12}$

DEFINITIONS

Ion: An atom or molecule with an electric charge (positive or negative) due to the loss or gain of electrons.

Doping: The introduction of controlled impurities into a material to alter some of its properties.

Ionic conductivity: Process in which ions move through a material; in the case of solid materials, through their crystalline structure or vacancies.

Crystalline structure: Orderly and repetitive arrangement of atoms, molecules or ions in a crystal.

Theoretical specific capacity: Maximum amount of electrical charge that a material can store per unit mass or volume.

Voltage: Electrical potential difference which drives the movement of electrons through a conductive material.

Vacancies: Defects in the crystal lattice due to the absence of an atom or ion in a given position.

Elemental charge: Electric charge (1.602×10^{-19} C) carried by an ion.

Coulombic repulsion: Repulsive force between particles with the same charge.

Sintering: Controlled heating of a material at temperatures close to its melting point to fuse its particles and form a solid structure.

Metal complex: Chemical species with a central metal atom or ion coordinated by covalent bonds with ligands.

Esterification: Chemical reaction between an acid and an alcohol in which an ester and water are formed.

Polyhydroxylated alcohol: Alcohols with more than one hydroxyl group (-OH) in their structure.

AC impedance spectroscopy: A technique that measures the impedance of a sample by applying an AC potential at different frequencies and measures the current.

Resistor: Electronic component used in electrical circuits to prevent the passage of electric current between two points.

Capacitor: Electronic component that stores energy by means of an electric field.

1. INTRODUCTION

In the last decades, lithium-ion batteries (LIBs) have dominated the market in terms of mobile power sources. They are considered the most advanced rechargeable batteries available to date, because of their high energy density, which makes them capable of meeting the demands for energy storage devices and electric vehicles [1-3]. According to the estimated data, approximately 100 GWh of energy from LIBs was needed to meet global consumption needs in 2018, of which 50% represents sales focused on electric vehicles [4].

Commercial lithium-ion batteries use organic liquid electrolytes, their high ionic conductivity (more than 10^{-2} S cm^{-1}) and good electrode wetting, ensures great battery performance. The energy density of current lithium-ion battery cell is 240 Wh/kg [5-7]. However, they present problems that can lead to safety risks, such as corrosion, leakage, and the possibility of exploding due to the flammability of the organic compounds in liquid electrolytes [5]. These problems have been accentuated by the growing consumer and industry need for safer and more durable devices, especially for the electric vehicle market [6].

The use of solid electrolytes made of conductive solid lithium-ion materials is an alternative with great potential for the next generations of LIBs. They can provide better safety by being non-flammable, having high-temperature durability, high mechanical integrity, and wide electrochemical operating voltage windows [8]. Among the different ceramic materials focused on solid electrolytes, $Li_7La_3Zr_2O_{12}$ (LLZO) based garnet-type have stood out for being good ionic conductors at room temperature (above 10^{-4} S cm^{-1}), having good electrochemical stability and a wide electrochemical potential window (0 - 5) [9].

LLZO has two crystalline phases: cubic garnet and tetragonal garnet. Among them, the cubic phase has received considerable interest, as it has a lithium-ion conductivity (10^{-3} - 10^{-4} S cm^{-1}) up to two or more orders of magnitude higher compared to the tetragonal phase (10^{-6} – 10^{-7} S cm^{-1}) [8]. However, the cubic phase of LLZO is difficult to synthesize and is not stable at room temperature, therefore research has focused on finding alternatives to mitigate these problems. Partial substitution or doping is considered an effective way to stabilize the cubic structure and improve the lithium-ion conductivity of the material by creating vacancies and disorder in the lithium sublattice [10-12]. Some commonly employed dopant cations are Ga^{3+}

or Al^{3+} at the Li^{+} sites; Ba^{2+}, Sr^{2+} or Ca^{2+} at the La^{3+} sites; and Nb^{5+}, Sb^{5+}, Ta^{5+} or Bi^{5+} at the Zr^{4+} sites.

The aim of this work is to synthesize LLZO garnet-type co-doped solid electrolytes with cubic crystal structure by the Pechini method. The experiment was divided into two stages. In the first stage, Li^{+} sites were partially substituted by Ga^{3+} in $Li_7La_3Zr_2O_{12}$, generating a series of $Li_{7-3x}Ga_xLa_3Zr_2O_{12}$ (x = 0, 0.1, 0.2 and 0.3). Subsequently, from the material with the best result in ionic conductivity, a second series was prepared for the second stage of the experiment, partially replacing Zr^{4+} by Gd^{3+} and obtaining the series of $Li_{7-3x+y}Ga_xLa_3Zr_{2-y}Gd_yO_{12}$ (y = 0.2, 0.4, 0.6 and 0.8). Finally, the obtained materials were subjected to characterization studies and ionic conductivity measurements to validate their behavior as solid electrolytes in lithium-ion batteries.

2. BACKGROUND

2.1 Batteries and sustainability

Currently, there is an environmental crisis induced by the growth of human activities that cause deterioration of the natural environment, such as industrial development, the massive exploitation of fossil fuels and the production and consumption of energy [13, 14]. Rechargeable batteries play a crucial role in meeting the energy needs related to mobility and energy storage, in a more sustainable way. It is estimated that meeting the energy demands of the world's population in 2050, will require the production of 130,000 TWh per year, equivalent to 10^{10} tons of oil [15]. Although several renewable energy sources can produce energy with a reduced carbon footprint, such as solar, wind, geothermal, etc., most of these systems are considered intermittent, with irregular periods of higher and lower production [15]. Therefore, it is necessary to develop devices capable of storing unused energy during periods of low demand to avoid unnecessary waste of resources, and to ensure supply during periods of high demand.

Climate change, a consequence of rising global temperatures, is mainly due to the emission of greenhouse gases (GHG). The transport sector is one of the main contributors to air pollution, accounting for 23% of the greenhouse gases emitted into the atmosphere [16]. For this reason, the automotive industry has focused its efforts on developing and implementing systems that can replace internal combustion engines, to reduce the environmental damage caused by the emission of polluting gases and reduce the use of fossil fuels. One of the main alternatives is electric vehicles (EVs), which have experienced a growing acceptance in the economic market. It is estimated that by 2030, 20% of vehicles on the road will be electric [16]. Figure 1 shows the increase in the ownership of electric vehicles in different countries.

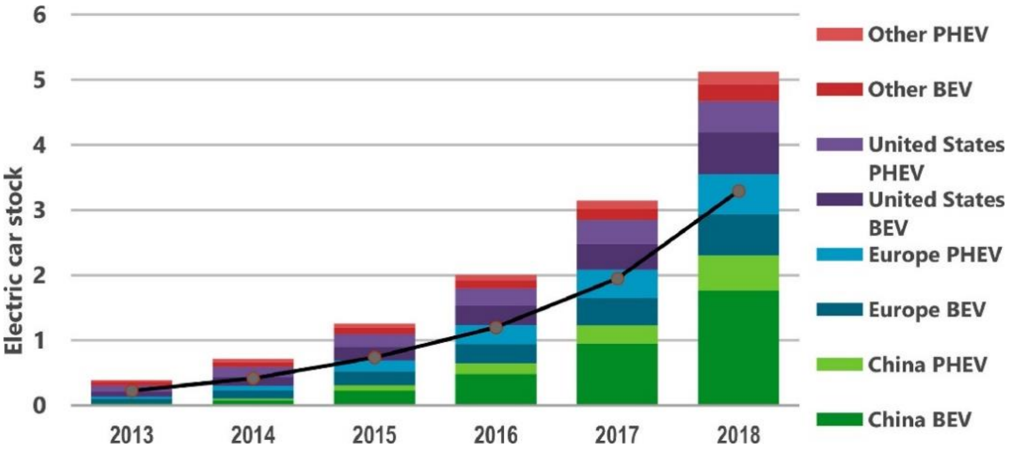

Figure 1. Increase in the ownership of electric vehicles in various countries [14].

EVs are of great interest because of their ability to reduce emissions. In the well-to-wheel study by Choi *et al.* [17] on the greenhouse gases emissions of electric vehicles, it was observed that in countries where oil imports predominate, the use of EVs resulted in a decrease in GHG emissions of 90-110 g CO_2 eq/km compared to oil-derived vehicles. Also, it is estimated that if the 35% of vehicles sold in 2030 are EVs, it would be possible to achieve the headline target of reducing global temperature by two degrees, as proposed in the Paris Declaration on "Electromobility and Climate Change and Call for Action" [18]. However, the development of EVs requires progress in energy storage devices, such as rechargeable batteries.

Batteries are the most common energy storage devices and, among the different types available, lithium-ion battery (LIB) dominates the rechargeable battery market, estimated to be worth $50 billion by the year 2050 [14, 19]. LIB´s are commonly used in a wide variety of applications due to their specific characteristics, such as: high energy density (from 120 -

220 Wh kg^{-1}); long lifetime due to the large number of charge/discharge cycles; and low weight [20, 21].

The commonly used electrolytes are organic liquids, which present certain safety risks due to their flammability and volatility [22]. In addition, they tend to be highly reactive towards the electrodes, producing secondary reactions, such as electrolyte decomposition, which affect battery capacity [23]. They also cause irreversible losses due to the formation of a stable solid electrolyte interface (SEI), and limits in the temperature window [24]. When using liquid electrolytes, the complexity of the assembly increases, requiring good packing to avoid leakage and a separator to avoid short circuits caused by the dendrite growth [22]. Some recorded cases of potential safety hazards arising from lithium-ion batteries in electronic applications. This includes the case of the Nokia brand in 2007, in which over 46 million batteries were recalled due to the risk of overheating and explosion. Similarly, in 2012 the Nikon camera company recalled more than 200,000 batteries due to risk of burns [25].

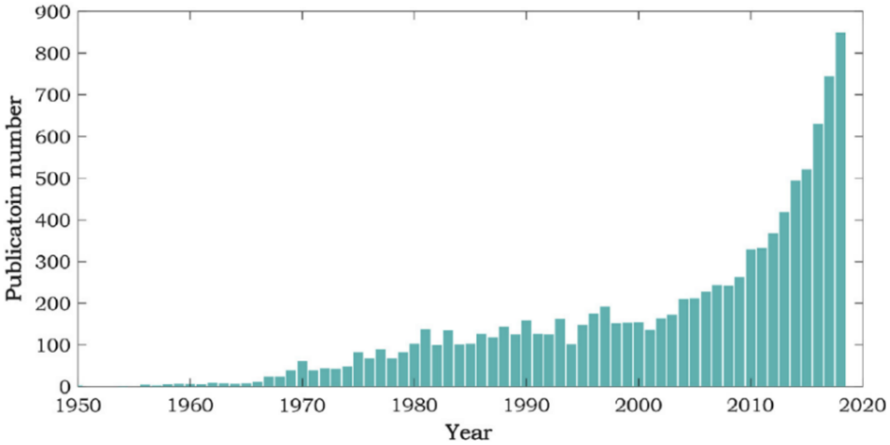

Figure 2. Number of registered publications per year, "using solid electrolyte" as a keyword in web of science database [26].

Solid electrolytes have emerged as a good alternative to solve most of the safety issues that arise when using liquid electrolytes in lithium-ion batteries [24]. In recent years, solid-state batteries have been considered as an alternative, with great potential, for the future development of cleaner energy storage devices; therefore, the number of research focused on the study of solid electrolytes (SE) has increased, as can be seen in Figure 2, which shows the annual growth rate of the number of registered publications related to solid electrolytes in the "web of science" database [26].

2.2 Solid-state lithium-ion batteries (SSLIBs)

The operating principle of a traditional LIB and a solid-state lithium battery is very similar. Both use a Li^+ ion intercalation/de-intercalation mechanism during charge/discharge cycles. During discharge, lithium ions de-intercalate from the anode material and travel towards the cathode, transporting through the electrolyte and electrode-electrolyte interface. In this process, electrons pass through an external circuit from the anode to the cathode. While charging, the mechanism is reversed [27]. Figure 3 shows the operation principle of a LIB cell.

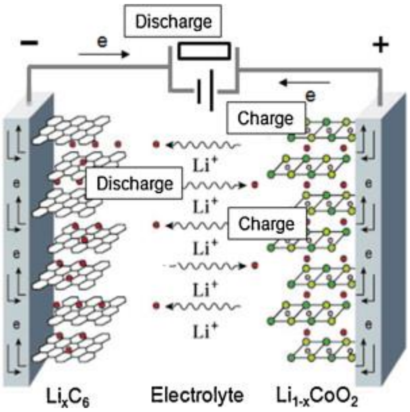

Figure 3. Schematic of the operation principle of a LIB cell [28].

The general reaction during the charging and discharging of LIBs, using a cathode based on transition metal oxides (M: transition metal) and a carbon anode, is described below.

$$\mathrm{Li_xC_6 + Li_{1-x}MO_2 \underset{\text{Charge}}{\overset{\text{Discharge}}{\rightleftharpoons}} C_6 + LiMO_2}$$

In solid-state batteries (SSB), the cell assembly consists of anode, solid electrolyte, cathode, and current connectors. Its main difference with traditional LIBs is the replacement of the porous separator impregnated with liquid electrolyte, by a solid electrolyte that acts as an ionic conductor and electrical insulator at the same time [26, 27, 29]. Figure 4 shows the comparative schematic diagram of a traditional lithium-ion battery cell and a solid-state battery cell.

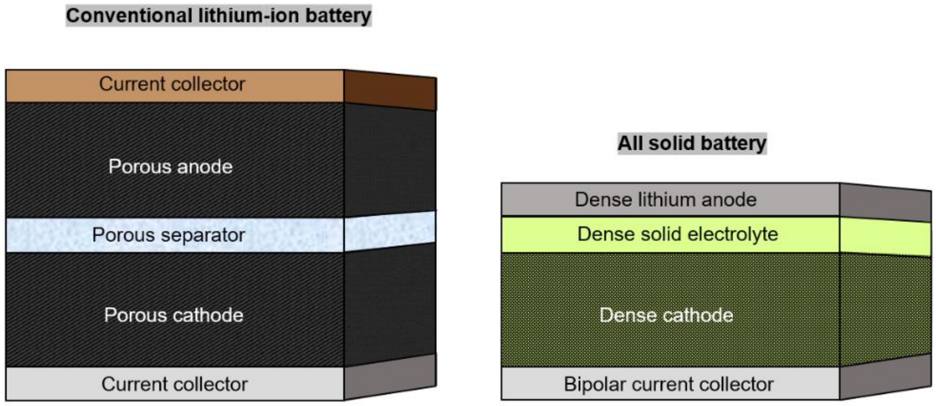

Figure 4. Comparative illustration of a traditional lithium-ion battery cell and a solid-state lithium-ion battery cell [29].

Solid-state lithium-ion batteries have a simplified structure compared to LIBs using liquid electrolytes. This simplification gives them smaller dimensions, up to 1/5 of their volume, which could lead to batteries with higher energy density. Moreover, by eliminating flammable liquids from the system, the manufacturing process is simpler [30, 31]. These characteristics in particular makes SSLIBs a great candidate for electric vehicle applications. The use of lithium metal as an anode in batteries is considered one of the most important approaches for the next generations of SSLIBs, due to its high theoretical specific capacity of 3860 mAh g^{-1}, i.e., the maximum amount of electrical charge that a material can store per unit mass or volume, compared to graphite, which is the currently used anode with a theoretical capacity of 372 mAh g^{-1} [9]. Using a solid electrolyte in SSLIB allows the use of a lithium metal anode, since, in addition to being chemically and electrochemically stable with lithium, it acts as a physical barrier for the formation of lithium dendrites [6, 29].

For a solid electrolyte to be considered suitable, it must meet certain requirements, such as:

I. High ionic conductivity (greater than 10^{-4} S cm^{-1}) over a wide temperature range, to obtain fast charge-discharge cycles and high-power values.

II. Negligible electronic conductivity, i.e., good electronic isolation to avoid self-discharge and short circuits.

III. Wide electrochemical stability window, which allows working at high voltages and ensures good stability to the electrolyte in contact with the electrodes.

IV. Good mechanical properties, to ensure system durability and cell performance [27, 29].

The two most important classes of materials used as solid electrolytes in SSLIBs are organic solid polymer electrolytes (such as: Li salts with high molecular weight polymers) and inorganic glassy/ceramics (inorganic electrolytes) [32]. Inorganic SEs tend to have a higher ionic conductivity at room temperature compared to polymer solid electrolytes, which can have values around 1×10^{-4} S cm^{-1} at temperatures between 60 - 80 °C [33]. Solid inorganic electrolytes can be classified into two types: oxides (e.g., Garnet-type, NASICON-type, Ge-based lithium phosphate and perovskites) and sulfides (e.g., thio-LISICON $Li_{3.5}Ge_{0.25}P_{0.75}S_4$, Li_6PS_5X (X = Cl, Br, I), $Li_{10}MeP_2S_{12}$ (M = Ge, Sn, Si) [32, 33]. Figure 5 shows the ionic conductivity of different types of solid electrolytes.

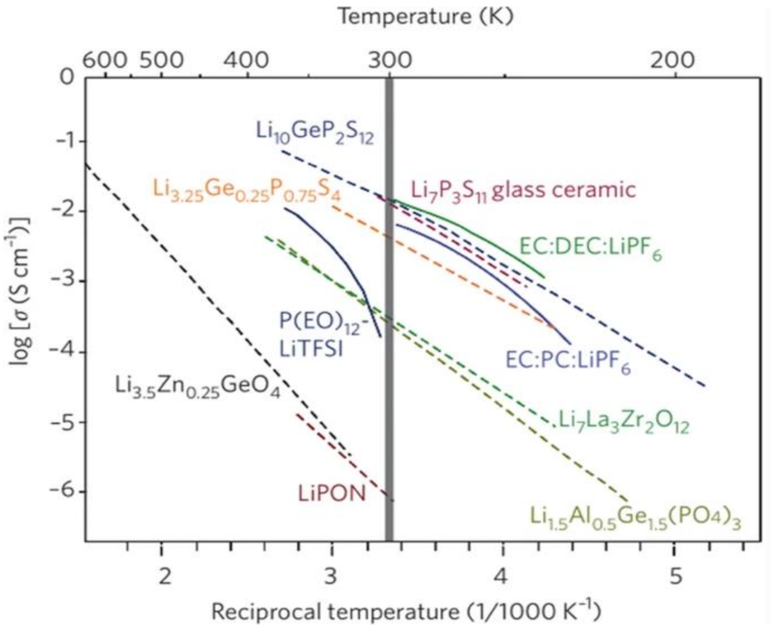

Figure 5. Arrhenius plot of various solid electrolytes (ionic conductivities vs temperature) [33].

Table 1. Different types of solid inorganic electrolytes and their ionic conductivity values [34].

Composition	Ionic conductivity
Oxysalts	
$Li_{1.4}Zn(GeO_4)_4$ (LISICON)	0.13 S cm^{-1} at 300 °C
$Li_{3.6}Si_{0.6}P_{0.4}O_4$ (thin film)	5×10^{-6} S cm^{-1}
$Li_{2.9}PO_{3.3}N_{0.46}$ (thin film, LiPON)	5×10^{-6} S cm^{-1}
Li_3BO_3	2×10^{-6} S cm^{-1}
Li_3BO_3–Li_2SO_4	1.4×10^{-5} S cm^{-1}
Li_3BO_3–Li_2CO_3	6.5×10^{-7} S cm^{-1}
NASICON type	
$Li_{1.3}Al_{0.3}Ti_{1.7}(PO_4)_3$	7×10^{-4} S cm^{-1}
$Li_{1.3}Al_{0.3}Ti_{1.7}(PO_4)_3$	3×10^{-3} S cm^{-1}
Perovskite type	
$Li_{0.34}La_{0.51}TiO_3$	1×10^{-3} S cm^{-1}
$Li_{0.33}La_{0.56}TiO_3$	1.2×10^{-3} S cm^{-1}
$Li_{0.29}La_{0.57}TiO_3$	1.6×10^{-3} S cm^{-1}
Garnet type	
$Li_7La_3Zr_3O_{12}$	5.1×10^{-4} S cm^{-1}
$Li_{6.75}La_3Zr_{1.75}Nb_{0.25}O_{12}$	0.8×10^{-3} S cm^{-1}
$Li_{6.4}La_3Zr_{1.4}Ta_{0.6}O_{12}$	1.0×10^{-3} S cm^{-1}
$Li_{6.25}Ga_{0.25}La_3Zr_2O_{12}$	1.46×10^{-3} S cm^{-1}

Sulfide solid inorganic electrolytes have the highest ionic conductivities at room temperature, with average values of 10^{-2} - 10^{-3} S cm^{-1}, while the ionic conductivities of oxide solid electrolytes range from 10^{-3} - 10^{-4} S cm^{-1} [33]. Some types of inorganic electrolytes and their respective ionic conductivity values are presented in Table 1.

2.3 $Li_7La_3Zr_2O_{12}$ (LLZO) garnet-type solid electrolytes

$Li_7La_3Zr_2O_{12}$ (LLZO) garnet-type ceramic materials are considered the solid electrolytes with the highest potential for SSBs due to their high ionic conductivity (10^{-4} - 10^{-3} S m^{-1}) and wide electrochemical potential (0 – 5 V) [30, 31]. Another advantage of garnet-type LLZO SEs is that they show good electrochemical stability towards lithium metal when acting as an anode material, compared to other ceramic materials. For example, NASICON $Li_{1.7}Al_{0.3}Ti_{1.7}(PO4)_3$ (LATP), which despite an ionic conductivity comparable to that of

LLZO SEs (~7×10^{-4} - 3×10^{-3} S cm^{-1}), tend to react with lithium metal, showing mechanical and thermal instabilities [31, 34].

The general formula of LLZO is $Li_7A_3B_2O_{12}$, corresponding to the family of the garnet-type structures, where Li^+ ions occupy octahedral and tetrahedral sites, while A and B cations belong to octahedral and hexahedra oxygen coordination crystallographic spaces [30, 35]. LLZO has two phases: t-LLZO tetragonal phase with the $I4_1$/acd space group and c-LLZO cubic phase with the Ia-3d space group. Both phases have the same structural framework but different distribution of Li atoms, t-LLZO has a completely ordered distribution of Li^+ ions, while c-LLZO has a deficiency of lithium, causing a disordered distribution of Li^+ ions and vacancies [36]. This difference determines the ionic conductivity of LLZO [35]. The cubic c-LLZO has higher ionic conductivity than the t-LLZO tetragonal phase since it has more sites available for Li^+ migration [35].

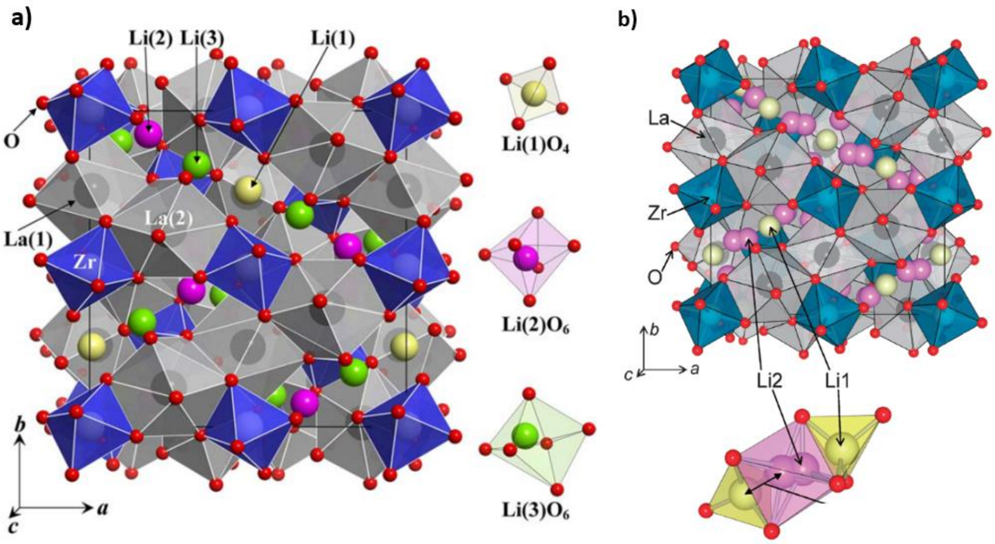

Figure 6. (a) Crystal structure of the tetragonal phase of $Li_7La_3Zr_2O_{12}$ (t-L*LZ*O) [38] and (b) Crystal structure of the cubic phase of $Li_7La_3Zr_2O_{12}$ (c-LLZO) [39].

LLZO cell with 8 per formula unit (pfu) has 56 lithium atoms, however, as can be seen in Figure 6, in t-LLZO, lithium ions can occupy tetrahedral 8a and octahedral 16f and 32g sites (L1, L2, L3). Therefore, it has only 56 sites available for lithium atoms, i.e., it has no empty spaces for Li^+ ion movement [35]. While in c-LLZO, lithium occupies two different sites: 24d tetrahedral and 96h octahedral (L1, L2), having 120 sites available for Li atoms, resulting in 64 empty spaces for Li^+ migration [35]. Due to this difference in ionic conductivity, the cubic phase of LLZO is considered more suitable for application as SE [37].

Since the preparation temperature of t-LLZO (950 °C) is lower than that of c-LLZO (1230 °C), a phase transformation by heating can take place [38].

2.3.1 Li-ion conduction mechanism in garnet-type solid electrolytes.

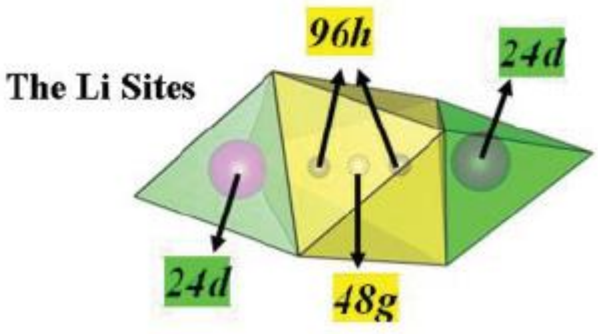

Figure 7. Li^+ distribution in the c-LLZO garnet electrolyte [40].

The Li^+ in the garnet structure is distributed in three different sites (Figure 7): 24d tetrahedral, 48g octahedral and 96h off-centered octahedral. In the case of c-LLZO, with more than 3 lithium atoms per formula unit, excess lithium is incorporated into the octahedral sites, which generates vacancies in the tetrahedral sites. This increase of lithium in the octahedra causes a shift of Li ions from the central 48g site to the off-center 96h site, due to the Li^+- Li^+ interaction [41].

For the migration mechanism in garnet materials, Baral *et al*. proposed two routes (Figure 8): in route A, Li octahedral sites do not participate in ion mobility, and Li^+ migrates between two octahedral sites through interstitials avoiding their common tetrahedral neighbor; in route B, octahedral and tetrahedral sites participate in the migration process, where Li^+ moves across shared faces and goes from octahedral to tetrahedral sites.

Recent studies reveal that ion diffusion in superionic conductors such as $Li_7La_3Zr_2O_7$ occurs through concerted migration of multiple ions with low-energy barriers, where several ions jump to the nearest neighbor sites [42].

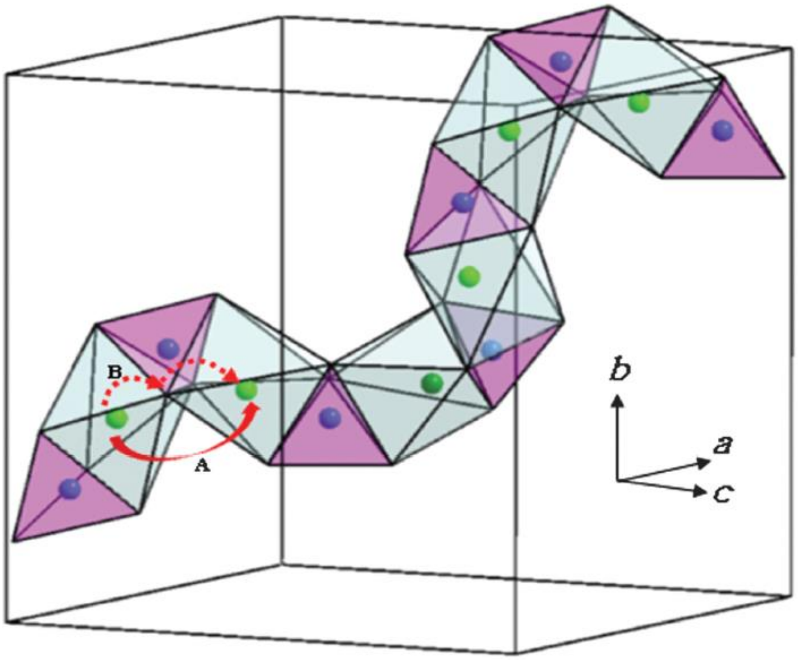

Figure 8. Schematic of the Li^+ migration mechanism in garnet materials [43].

2.3.2 Doping in $Li_7La_3Zr_2O_{12}$ garnet-type SEs

The cubic phase of $Li_7La_3Zr_2O_{12}$ exhibits thermodynamic instability at room temperature, i.e. a tetragonal structural arrangement is more favorable under these temperature conditions, however, partial substitution of Li, La and Zr sites has been shown to be effective for the stabilization of c-LLZO [44, 45]. Moreover, certain factors during the synthesis, such as sintering temperature, can affect the microstructure of the material (effects on the crystalline structure, grain boundaries, density, etc.), decreasing the conductivity of LLZO SEs [30]. Different works have been reported, using Al and Ga substituents, on Li sites; Sr, Ce, on La sites; and Ta, Nb, Te, and W on Zr sites, which have been shown as effective dopants to achieve the stability of the cubic phase of LLZO, also promoting an increase in the ionic conductivity of the material [44, 45, 46].

The ionic conductivity (Equation 1) of a solid electrolyte can be expressed from the following factors: the elemental charge (q), which refers to the electric charge (1.602×10^{-19} C) carried by an ion; the concentration of mobile ions (η_C); and the mobility of ions within the crystal structure (μ). These last two parameters can be modified by the introduction of heterovalent ions [36].

$$\sigma = q \cdot \eta_C \cdot \mu \quad (1)$$

In LLZO, the concentration of vacancies is higher than that of mobile Li^+ ions, because most of the Li^+ is trapped. However, by doping in La^{3+} sites, the size of the ion migration pathway can be enlarged, allowing a higher mobility of ions through the material [36, 47]. In addition, during ion migration, coulombic interactions exist due to the small separation in the crystal structure. Among these interactions, the Coulombic repulsion that exists between Li^+ and dopants such as Ga^{3+}, Al^{3+} Zn^{2+} is greater than that present in Li-Li interactions. The increased repulsion can activate lithium ions, altering the concentration and mobility of the migrating ions and therefore improving the ionic conductivity [36].

Wu *et al.* [36] investigated the influence of Ga as a dopant on LLZO by generating a series of $Li_{7-3x}Ga_xLa_3Zr_2O_{12}$ (x = 0.10, 0.15, 0.20, 0.25, 0.30, 0.35 and 0.40), by solid-state reactions as a synthesis method. In this work, it was reported that x ≥ 0.20 of Ga, the stabilization of the cubic phase of LLZO was achieved, while at lower doping values, both phases (tetragonal and cubic) coexisted. The highest ionic conductivity obtained was 1.46×10^{-3} S cm^{-1} at 25 °C with x = 0.25 of Ga per formula unit. In 2019, the best result obtained in terms of ionic conductivity (1.30×10^{-4} S cm^{-1}) was achieved by partial substitution of Li sites by Ga, in a $Li_{6.40}Ga_{0.2}La_3Zr_2O_{12}$ structure [44]. Wu *et al.* [48] studied the effect of co-doping in the cubic phase of $Li_{6.10}Ga_{0.30}La_3Zr_2O_{12}$, substituting La^{3+} sites by Rb^+, and obtaining $Li_{6.10}Ga_{0.30}La_{2.95}Rb_{0.05}Zr_2O_{12}$. The ionic conductivity obtained was 1.62×10^{-3} S cm^{-1} at room temperature and 4.56×10^{-3} S cm^{-1} at 60 °C.

Doping the Zr^{4+} sites with lower valence elements (two- and three-valent ions) can stabilize the cubic LLZO phase. This addition also modifies its lithium-ion stoichiometry, leading to an increase in Li^+ carriers, causing an enhancement of the ionic conductivity [49]. Despite the difference in the size of the atomic radio with hexahedral coordination of Zr^{4+} (0.72 Å) and Gd^{3+} (0.96 Å), the partial substitution of Zr sites in the LLZO structure by Gd is considered feasible [50]. Gd-doped LLZO was first reported in 2018 by Song *et. al.* [50], where they successfully synthesized a series of $Li_{7+x}La_3Zr_{2-x}Gd_xO_{12}$ (x = 0, 0.1, 0.2, 0.3, 0.4, 0.5) in cubic phase via solid-state reactions. In this work, it was concluded that Zr^{4+} substitution with Gd^{3+} concentrations of $x < 0.2$ increases the total ionic conductivity of $Li_7La_3Zr_2O_{12}$, reaching the highest result of 2.3×10^{-4} S cm^{-1} at room temperature.

Subsequently, Luo *et al.* [51] investigated the effect of co-doping on the LLZO solid electrolyte by carrying out a double substitution with Nb^{5+} and Gd^{3+} at the Zr^{4+} sites forming $Li_{7-x+y}La_3Zr_{2-x-y}Nb_xGd_yO_{12}$ ($x = 0.6$; $y = 0, 0.056, 0.1, 0.2$), by solid-state reactions. All the synthesized samples showed a cubic structure, good ionic conductivities, and stability towards metallic Li as an electrode. The maximum conductivity value recorded for the Nb and Gd doped LLZO was 9.86×10^{-4} S cm^{-1} at room temperature.

2.3.3 Synthesis methods of garnet-type $Li_7La_3Zr_2O_{12}$ SEs

There are several synthesis methods to obtain pure and doped LLZO. Among them, the most common method is the solid-state reaction~~s~~, which involve ball milling and sintering. However, this method requires high temperatures, so it involves high energy consumption and can lead to lithium losses [30, 35]. The sol-gel method is another synthesis mechanism to obtain LLZO, in which hydrolysis and polymerization reactions are carried out. Its main advantage is that it allows to obtain good ionic conductivities at lower sintering temperatures compared to that of solid-state reactions, avoiding Li loss. In addition, it does not require grinding mechanisms to obtain fine particles with uniform distribution [30, 35].

The Pechini method, also known as complex polymerization method, is a modification of the sol-gel method in which carboxylic acids are used to chelate metal ions and form a polymer resin when heated with some hydroxy alcoholic agent (such as polyethylene glycol) [35]. This method requires low sintering temperatures compared to solid-state reactions and thus shorter times. Moreover, like the sol-gel method, it produces fine powders with uniform distribution without requiring additional milling processes [35, 52]. Kokal *et. al* [53] succeeded in completely synthesizing polycrystalline c-LLZO powders ($Li_7La_3Zr_2O_{12}$ cubic phase) at low temperature (700 °C), by the Pechini method, using citric acid as chelating agent and ethylene glycol as organic solvent.

2.3.4 Pechini method.

This methodology is named after the author of the original 1967 patent [54]. The main chemistry involved is related to the formation of metal complexes and subsequent esterification of the carboxylic acid and polyhydroxylated alcohol after heating [54, 55].

In a usual Pechini synthesis, the metal salts are dissolved in water with citric acid and ethylene glycol (the most used carboxylic acid and polyhydroxy alcohol) to form a homogeneous precursor solution. In the beginning of the synthesis, as shown in Figure 9a, chelation of the cations (from the dissolution of the salts) with the carboxylic acid takes place. This process leads to the formation of a homogeneous solution of metal complexes [55]. Upon heating, citric acid (free and complexed) and ethylene glycol initiate the polyesterification of the metal complexes, producing a polyester resin, in which the metal ions are bound to organic radicals. In this process, ethylene glycol also acts as a chelating agent, ensuring that all metal ions are completely bound [56]. Figure 9b shows the esterification reaction between citric acid and ethylene glycol in the Pechini synthesis [56, 54].

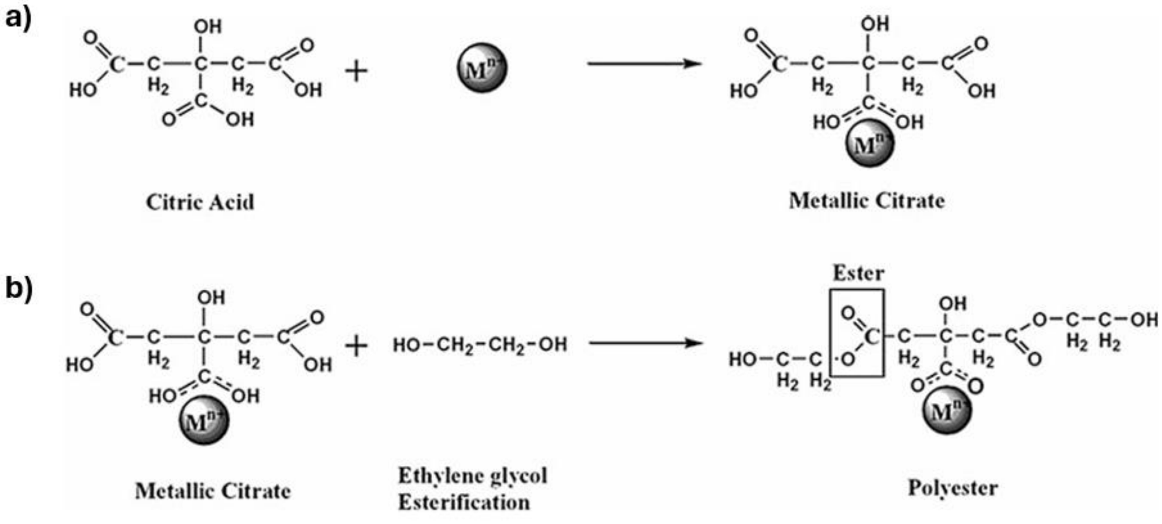

Figure 9. Scheme of the Pechini method reactions [57].

After the formation of the polymeric structure, the resulting material is heated to burn out the organic matrix and form the ceramic product. An important aspect of this method is the immobilization of the metal complexes in the rigid polyester matrix to preserve the same ratio of metal ions during polymerization [54]. Figure 10 shows the general process of the Pechini synthesis.

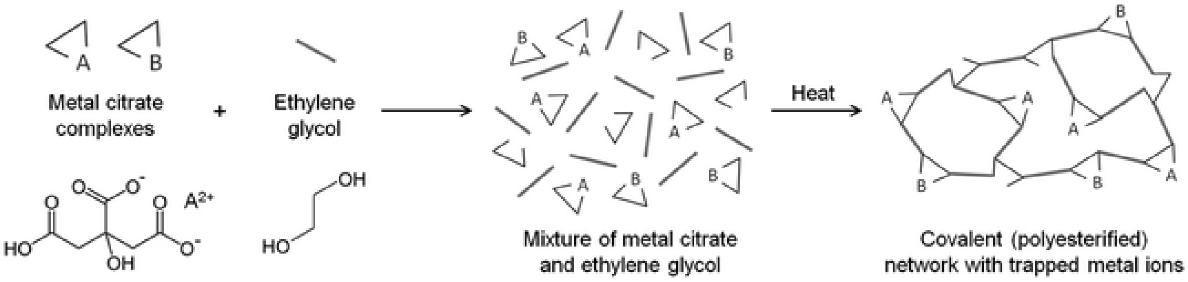

Figure 10. Scheme of the Pechini method process [55].

2.4 AC impedance spectroscopy

AC impedance spectroscopy is a non-destructive technique that involves the analysis of electrical materials, such as liquid and solid electrolytes [58]. In solid electrical materials, the properties to be measured can be divided into four categories: bulk properties; grain boundary properties; combination of bulk and grain boundary properties; and surface properties. AC impedance analysis is one of the most convenient methods to evaluate each of the individual components of the material separately and provides a lot of information of the physical and electrochemical process that occurs [59].

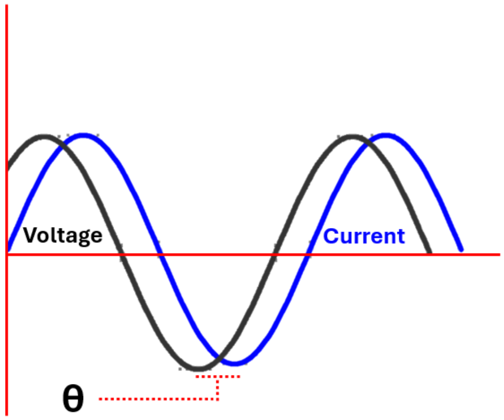

Figure 11. Diagram of sinusoidal signal and its response.

Impedance analysis is based on the application of a sinusoidal signal (Figure 11) to the system (AC current or AC voltage) over a wide frequency range (from 10^{-4} Hz to 10^{7} Hz) and the measure of the received sinusoidal response (AC current or AC voltage). There is usually a phase shift between the applied and received signal, known as "θ" [60, 61].

The Nyquist plot is the most used representation for AC impedance data, showing the impedance in terms of its real and imaginary components on the horizontal and vertical axes, respectively. [62]. Each point on the Nyquist plot corresponds to an impedance value at its corresponding frequency. In this type of plot, the impedance can be represented as a vector |Z| and its angle within the x-axis is the phase angle [62].

In an ideal case, the shape of a Nyquist plot consists of a semicircle with its center on the real axis as shown in Figure 12. The frequency increases from right to left as indicated by the arrow. However, the case is different in the non-ideal or real systems, where a depressed semicircle with its center below the real axis due to the inhomogeneities in the sample. In a non-ideal case, the shape of Nyquist plots depends on the arrangement and nature of the systems evaluated. However, an ionic conducting material usually has semicircles in the high, and intermediate frequency ranges, assigned to bulk and grain boundary contributions, and a tail in the low frequency range in the case of ion-locked electrodes [63].

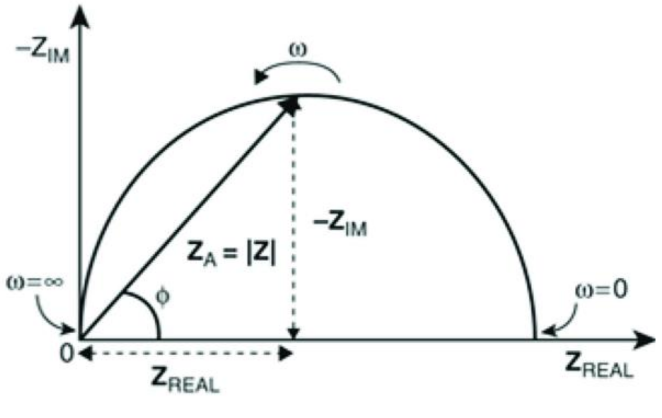

Figure 12. The schematic of a typical Nyquist plot [62].

To evaluate the individual components of an electrochemical impedance system, an electrical circuit with electrical components (resistors, capacitors, etc.) is used to match the experimental data [62].

3. JUSTIFICATION

Currently, lithium-ion batteries are widely used in portable electronics, electric vehicles and energy storage due to the intermittent of energy production systems. However, they have complications in terms of safety, due to the use of organic liquid electrolytes. These complications are leakage of the liquid electrolyte, overheating and danger of explosion due to the flammable compounds they contain. Therefore, the use of solid electrolytes to develop lithium-ion batteries has emerged as a good alternative to solve most of the mentioned problems. Among the different materials studied, $Li_7La_3Zr_2O_{12}$ garnet-type structures are considered as one of the most promising solid electrolytes, due to their high ionic conductivity, wide electrochemical potential window, and good stability against metallic Li.

However, the substitution of aliovalent elements can alter the ionic conductivity of LLZO. The partial substitution of certain atoms in the LLZO structure has been shown to be a good alternative to stabilize the high conducting cubic phase and increase the ionic conductivity of the material.

In this project, we intend to synthesize co-doped garnet type material based on LLZO by Pechini method, to study the effect of partial substitution on the structure and electrical properties of the material. This synthesis method has the advantage of using lower sintering temperatures than those required in the conventional high-temperature solid state synthesis. By using lower temperatures, the synthesis becomes less energetically demanding and with low lithium losses. Similarly, it is expected that by the partial addition of Ga^{3+} and Gd^{3+} substituents at the Li^{+} and Zr^{4+} sites, the cubic phase of LLZO can be obtained, and therefore leads to an increase in the ionic conductivity of the material. Obtaining solid electrolytes with high ionic conductivities means that there is a better flow of lithium ions through the battery, resulting in systems with higher charge/discharge efficiencies and higher energy storage capacities.

4. OBJECTIVES

4.1. General objective

To develop garnet-type solid electrolyte based on $Li_7La_3Zr_2O_{12}$ using the Pechini method and analyze the influence of co-doping Ga^{3+} and Gd^{3+} on the Li and Zr site impedance spectroscopy for SSLIB applications.

4.2 Specific objectives

- To demonstrate the feasibility of obtaining garnet structured $Li_7La_3Zr_2O_{12}$ ceramic materials by the Pechini method.
- To achieve the stabilization of the cubic phase at low temperatures in Ga and Gd doped garnet electrolyte by varying the concentrations in the composition $Li_{7-3x+y}Ga_xLa_3Zr_{2-y}Gd_yO_{12}$, where $x = 0, 0.1, 0.2, 0.3$; and $y = 0.2, 0.4, 0.6$ and 0.8.
- Investigate the impact of doping on the crystal structure and microstructure of the electrolyte by different characterization techniques (XRD, SEM, FTIR and TGA-DSC).
- To achieve dense materials by adequate sintering to evaluate their electrical properties.
- Examine the electrical properties by impedance spectroscopy to detect how the co-doping of Ga and Gd at the Li and Zr sites influences the ionic conduction.
- To identify and document key results related to the influence of co-doping on the structure and ionic conducting properties of LLZO garnet solid electrolytes.

5. METHODOLOGY DOPED SAMPLES

In this work, the Pechini method was used for the synthesis of doped $Li_7La_3Zr_2O_{12}$ (LLZO) garnet type solid electrolyte. The general procedure is carried out in two stages:

I. Synthesis of Ga-doped $Li_{7-3x}Ga_xLa_3Zr_2O_{12}$ garnet oxides.
II. Synthesis of co-doped $Li_{7-3x}Ga_xLa_3Zr_{2-y}Gd_yO_{12}$ garnet oxides. After each stage, characterization studies and ionic conductivity measurements are carried out.

The precursors employed included $C_2H_3LiO_2$ (98.7%), $La(NO_3)_3·xH_2O$ (99.9%), $ZrO(NO_3)_2·xH_2O$ (99%), $Ga(NO_3)_3·xH_2O$ (99.9%), and $Gd(NO_3)_3·xH_2O$ (99.99%). Additionally, ethylene glycol and citric acid ($HOC(COOH)(CH_2COOH)_2$) were utilized as complexing agents. All reagents were obtained from Sigma Aldrich.

5.1 Synthesis of Ga-doped $Li_7La_3Zr_2O_{12}$ garnet oxides

The methodology used for the synthesis of garnet oxides was the one described by [45], with some modifications. $Li_{7-3x}Ga_xLa_3Zr_2O_{12}$ series was prepared by changing the Ga concentrations to x = 0, 0.1, 0.1, 0.2 and 0.3. The corresponding amounts of each reagent are given in Table 2. An excess of lithium (10%) was added to compensate for the Li loss during high temperature treatments. The citric acid was added in a 1:4 ratio with ethylene glycol. In all synthesis, 200 mL of deionized water was used to obtain 7 g of LLZO powder.

Table 2. Amounts of reagents used for the synthesis of 7 g of Ga doped LLZO.

Reagents	**Amount (g)**			
	x = 0	x = 0.1	x = 0.2	x = 0.3
$C_2H_3LiO_2$	3.8501	3.6637	3.4795	3.2975
$La(NO_3)_3·xH_2O$	10.8285	10.7658	10.7038	10.6426
$ZrO(NO_3)_2·xH_2O$	5.6270	5.5945	5.5622	5.5304
$Ga(NO_3)_3·xH_2O$	--	0.3403	0.6767	1.009
Citric acid	19.2178	18.7881	18.3633	17.9435
Ethylene glycol	12.4177	12.1401	11.8656	11.5943

Two 1 L beakers were used, and 100 mL of deionized water was taken in each beaker. Citric acid was added to one of the beakers, while in the other one, all the nitrate salts were added in stoichiometric proportion. Both mixtures were placed on magnetic stirrers and mixed until complete homogenization occurs.

Then, the ethylene glycol is added dropwise to the nitrate salt mixture and stirred for 24 h, with an aluminum lid placed over the container to prevent leaks. After that, without interrupting the agitation, the temperature was raised to 100 °C. After one hour, the temperature was increased at a rate of 30 °C for every 20 min. Stirring was stopped at 270 °C and the temperature increased to 300 °C. Heating was continued until all the water evaporated and brown powder was formed. The material was then subjected to preheating in a muffle furnace at 600 °C for 3 h at a heating rate of 3 °C/min. Subsequently, the preheated powders were ground using a mortar and pestle and calcined at 875 °C for 6 h at a heating rate of 3 °C/min. After this step, the calcined powders were ground finely and made pellets using 0.2 g pressed at 1.3 Ton/m^2, using a CARVER hydraulic press. The dimensions of the pellets obtained are 6 x 1 mm in diameter and thickness, respectively.

The pellets were subjected to sintering at 1100 °C at a heating rate of 2 °C/min for 12 h, in MgO crucibles to avoid potential aluminum contamination from the alumina crucibles during sintering. Also, 2 g of the mother powder (MP) of the same composition was used to cover the surface of the pellets to reduce the loss of lithium at high temperatures (Figure 13). The obtained ceramic pellets and powders are stored in a desiccator during characterizations.

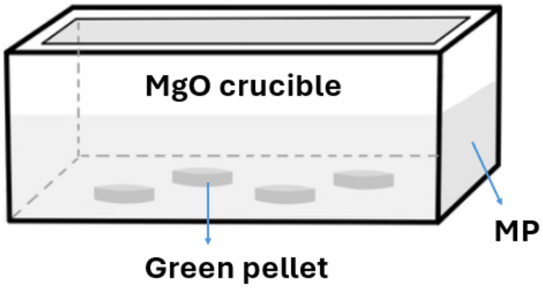

Figure 13. Sintering setup with mother powder in the MgO crucible.

5.2 Synthesis of co-doped $Li_7La_3Zr_2O_{12}$ garnet oxides

For the second stage of this work, the same methodology used for the doped samples was employed. To evaluate the effect of Gd on the samples, characterization studies and ionic conductivity measurements were carried out. The Ga concentration with x = 0.2 exhibited the best results, therefore the same sample was used for the second series.

$Li_{6.1+y}Ga_{0.2}La_3Zr_{2-y}Gd_yO_{12}$ series was prepared by changing the Gd concentrations y = 0.2, 0.4, 0.6 and 0.8. The corresponding amounts of each reagent are given in Table 3. An excess of lithium (10%) was added to compensate for the Li loss during high temperature treatments. The citric acid was added in a 1:4 ratio with ethylene glycol.

Table 3. Amounts of reagents used for the synthesis of 7 g of co-doped LLZO.

Reagents	**Amount (g)**			
	x = 0.2	x = 0.4	x = 0.6	x = 0.8
$C_2H_3LiO_2$	3.5741	3.6213	3.6669	3.7110
$La(NO_3)_3{\cdot}xH_2O$	10.3232	10.1518	9.9859	9.8254
$ZrO(NO_3)_2{\cdot}xH_2O$	4.9633	4.3385	3.7342	3.1493
$Ga(NO_3)_3{\cdot}xH_2O$	0.4911	0.4829	0.4750	0.4674
$Gd(NO_3)_3{\cdot}xH_2O$	0.7299	1.4357	2.1184	2.7791
Citric acid	18.3645	18.3666	18.3633	18.3677
Ethylene glycol	11.8664	11.8678	11.8656	11.8684

5.3 Physicochemical characterizations

A series of characterization techniques were performed on the synthesized samples.

1) X-ray diffraction

To identify the crystalline phase of all calcinated and sintered samples, XRD tests were carried out on a Philips Xpert PW3040 diffractometer. Scans were made from 10 to 80° 2θ, using Cu Kα radiation (1.541 Å).

2) Field Emission Scanning Electron Microscopy (FE-SEM)

For the Ga- doped samples, a JEOL JSM 7800f Prime microscope was used to characterize the surface morphology and microstructure of the sintered pellets. In addition, an Energy Dispersive X-ray spectroscopy (EDX) was used to determine the chemical composition of the materials.

3) Scanning Electron Microscopy (SEM)

In the co-doped samples, SEM were performed in an ESEM PHILIPS XL 30, under an accelerating voltage of 15 and 20 kV, to characterize the surface morphology and microstructure of the sintered pellets. In addition, an EDAX GENESIS system was used, with an accelerating voltage of 20 kV to determine the chemical composition of the materials. The change of SEM equipment between doped and co-doped samples is due to unavailability of FE-SEM, as the equipment was out of service at the time of the second stage of experimentation.

4) Thermogravimetry analysis and differential scanning calorimeter (TGA/DSC)

The thermal properties of the LLZO powders (pre-heated) were obtained with a thermogravimetric analysis (TGA) and a differential scanning calorimeter analysis (DSC). The analysis was carried out using TA Instruments, Waters, LLC, USA, from room temperature to 1200 °C with a heating rate of 5 °C/min in air.

5) Fourier Transform Infrared Spectroscopy (FT-IR)

FTIR spectra were obtained using the PERKIN ELMER FRONTIER spectrometer using an ATR accessory, in the range of 500-4000 cm^{-1} with a resolution of 4 cm^{-1}.

5.4 Electrical conductivity measurement

Before the electrical conductivity measurements, the density of the sintered pellets was calculated by Archimedes method using an Ohaus Adventurer Pro II density determination kit. Subsequently, the sintered pellets were polished with 1200 grits sandpaper to smooth the surfaces and reduce the thickness, alcohol was used to clean external impurities. Then, both sides of the pellets were painted with a silver paste. Finally, they were placed in a muffle furnace at 600 °C for 1 h at a heating rate of 5 °C/min to remove the organic contents in the paste. The electrical conductivity measurement was carried out using a Solartron 1260 impedance analyzer in the frequency range of 1 Hz to 10 MHz in air. The impedance measurements were recorded in 25 °C increments, using a homemade furnace to heat the samples in the temperature range of 25 °C to 200 °C.

After obtaining the impedance plots, an equivalent circuit was used to fit the experimental data, the fitting was performed using Zview software. The total ionic conductivity was calculated using the total resistance obtained from the fit and the following equation:

$$\sigma_{Total} = \frac{t}{R_{Tot} * A} \qquad (2)$$

Where:

σ_{Total} = total ionic conductivity (S/cm).
A = cross − sectional area of the sample (cm^2).
t = thickness of the pellet (cm).
R_{Tot} = total resistance (bulk + grain boundary resistance) (ohm)

The activation energies were estimated from the correlation of the temperature with the calculated conductivity. This can be described by using the Arrhenius equation (Equation 3).

$$\sigma = \sigma_0 exp\left(\frac{-E_a}{K_B T}\right) \qquad (3)$$

where:
σ_0 = Pre-exponential factor of the dc conductivity (S cm^{-1})
E_a = Activation energy for the mobile ions (kJ/mol)
K_B = Boltzmann´s constant (1.380649×10^{-23} JK^{-1}).
T = absolute temperature (°K).

The density of the sintered pellets was calculated based on Archimedes' principle, which describes that a solid loses weight when immersed in a fluid in proportion to the amount of liquid it displaces. For the measurement, a density kit coupled to the Ohaus balance was used and the immersion liquid was ethanol, since its density at different temperatures is known. Finally, the weight of the pellets, in and out of the liquid, were measured and the density was obtained from the following equation:

$$\rho = \frac{A}{A-B}(\rho_0 - \rho_L) + \rho_L \qquad (4)$$

Where:

ρ = Density of sample
A = Weight of sample in air
B = Weight of sample in the auxiliary liquid
ρ_0 = Density of the auxiliary liquid
ρ_L = Air density (0.0012 g/cm^3)
α = Balance correction factor (0.99985), takes air buoyancy of the adjustment weight into account.

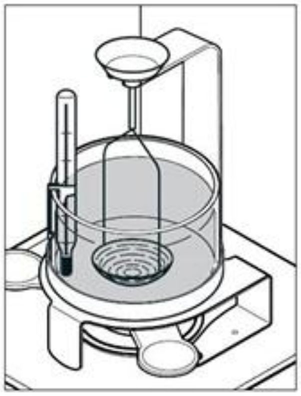

Figure 14. Ohaus density kit.

6. RESULTS AND DISCUSSION

6.1 DOPED SAMPLES

6.1.1 TGA/DSC analysis

Figure 15 shows the TGA/DSC curves of $Li_{7-3x}Ga_xLa_3Zr_2O_{12}$ ($x = 0, 0.1, 0.2$ and 0.3) samples from room temperature to 1100 °C in air. Powders preheated at 600 °C for 1 h were used for the analysis. All the TGA plots show three weight loss stages. An initial weight loss occurred at temperatures below 300 °C may be related to the release of adsorbed H_2O due to interaction with ambient humidity [8]. In the case of pure LLZO and 0.1 doped ($x = 0, 0.1$), the second stage of weight loss occurred around 300 to 600 °C and is due to the evaporation of the reagents. The last stage of weight loss occurs from 600 to 800 °C and can be attributed to the degradation of the residual organic compounds. In the DSC plot of $x = 0$ (Figure 15A), the exothermic peaks shown at 294 and 457 are attributed to the evaporation of H_2O and reagents. The exothermic peak seen at 723 °C, which coincides with a weight loss of 27% can be assigned to the degradation of residual organic compounds. The weight loss becomes negligible around 900 °C, indicating the transformation of the precursors into garnet oxides and the last exothermic peak observed at 905 °C corresponds to the transition to the tetragonal structure [53].

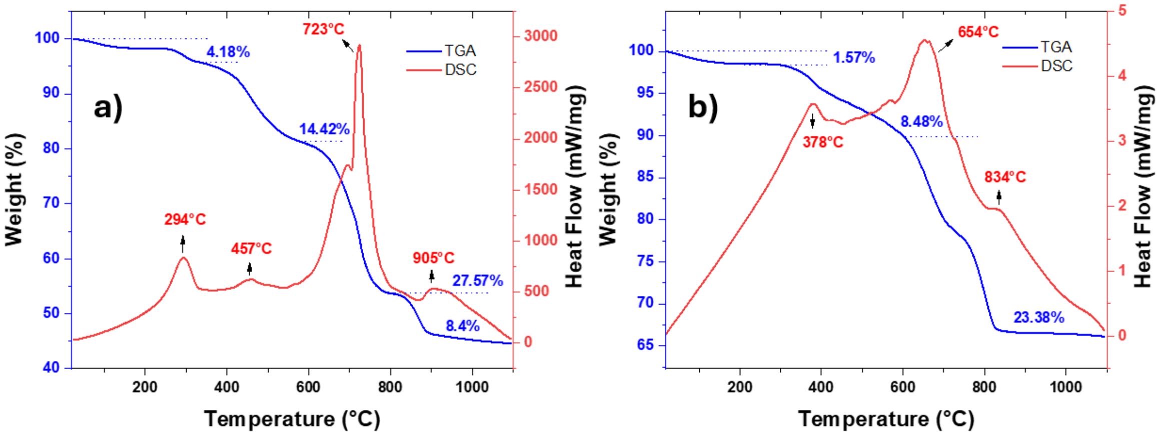

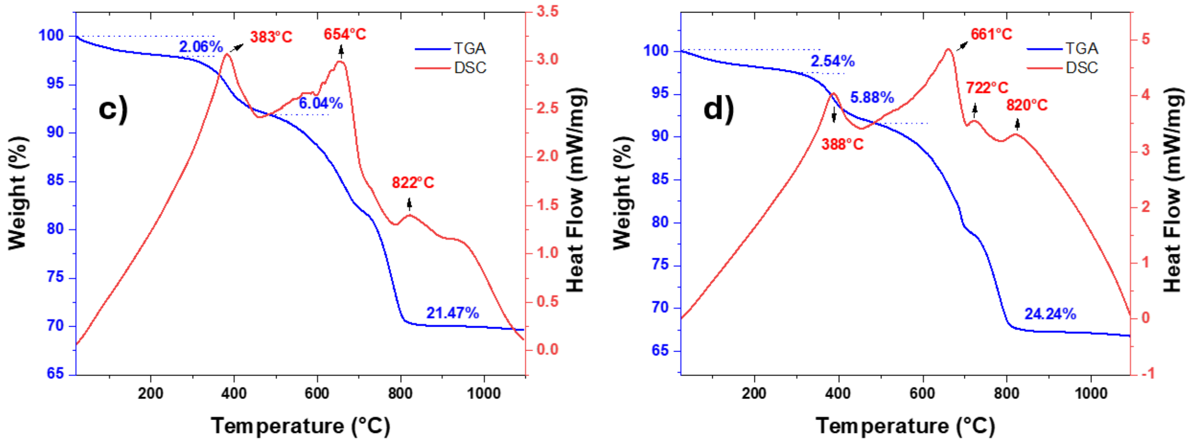

Figure 15. TGA-DSC curves for the $Li_{7-3x}Ga_xLa_3Zr_2O_{12}$ powders preheated at 600 °C, (a) x = 0, (b) x = 0.1, (c) x = 0.2 and (d) x = 0.3.

Exothermic peaks in the sample x = 0.1 are shown at different temperatures compared to pure LLZO, the exothermic peak attributed to evaporation of the reagents is shown at 378 °C, and the exothermic peak at ~654 °C is attributed to degradation of residual organic compounds [53]. The weight loss becomes negligible around 800 °C. The final exothermic peak at 834 °C corresponds to the formation of the tetragonal LLZO phase as observed in the XRD results.

For the samples doped with x = 0.2 and x = 0.3 (Figures 15c and 15d), the weight losses occur at different temperatures, the second stage starts around 300 °C to 450 °C and the last stage is from 450 °C to 800 °C. DSC analysis plots of the samples show three broad exothermic peaks. The peaks observed around 385 and 654 °C are attributed to the same processes described for x = 0.1 sample. The TGA plots show that above 800 °C the weight loss is negligible, indicating the transformation of the precursors into garnet oxides, so that the exothermic peak around 821 °C corresponds to the formation of cubic LLZO, which agrees with the results obtained by XRD [53].

The pure LLZO sample (x = 0) shows a negligible weight loss after 900 °C, whereas the doped samples exhibited a negligible weight loss after 800 °C. The thermal analysis results together with the XRD analysis indicate that the undoped sample requires a higher temperature to achieve the garnet-like structure compared to Ga doped samples.

6.1.2 X-ray diffraction

Figure 16 shows the XRD patterns of all calcined and sintered $Li_{7-3x}Ga_xLa_3Zr_2O_{12}$ samples. All diffraction peaks of the samples with x = 0 and 0.1 are indexed to a pure tetragonal phase after calcination at 875 °C. The cubic phase with a space group *Ia-3d* (black lines in Figure 16, PDF - 04 - 019 – 8837) in these two compositions is only obtained after sintering at 1100 °C. However, a cubic LLZO phase is achieved for x = 0.2 and 0.3 samples with only a low calcination temperature of 875 °C (Figure 16a), and even after sintering at a high temperature of 1100 °C, the diffraction peaks corresponding to cubic phase remains the same without the presence of any impurity (Figure 16b).

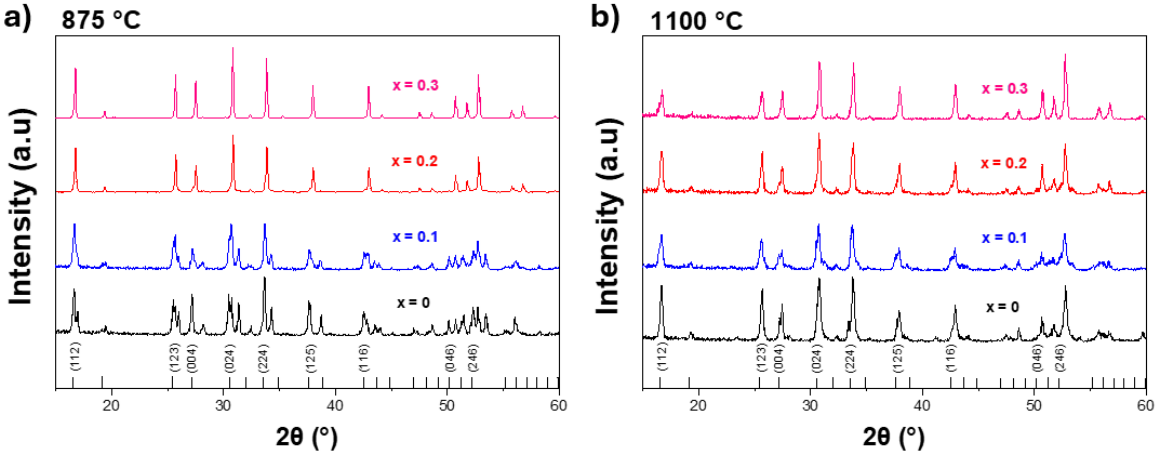

Figure 16. XRD patterns of $Li_{7-3x}Ga_xLa_3Zr_2O_{12}$ (x = 0, 0.1, 0.2 and 0.3) samples (a) calcined at 875 °C and (b) sintered at 1100 °C.

Vacancies in the crystalline structure of LLZO are the key to the stabilization of c-LLZO. According to the crystal chemical reaction, Ga is substituted into the Li site as shown in equation 5, where $2Ga_{Li}$ has an effective charge of +2 and represents the occupancies of Ga^{3+} in the Li^{+} site. Consequently, it forms vacancies with a charge of -1. ($4V_{Li}$) to maintain charge equilibrium with the oxygen lattice [64].

$$Ga_2O_3 \rightarrow 2Ga_{Li}^{\cdot\cdot} + 4V'_{Li} + 3O_O^{x} \qquad (5)$$

Recent studies have determined that a Li vacancy concentration of 0.4 - 0.5 per unit LLZO formula is required to stabilize the cubic structure, for this to be achieved, the critical amount of gallium substitution in the Li-sublattice is Ga ≈ 0.2 [65].

These XRD results, together with TGA/DSC analyses, demonstrate the stabilizing effect of Ga-doping to obtain the cubic structure in $Li_7La_3Zr_2O_{12}$ at low temperature due to the formation of vacancies.

6.1.3 Fourier Transform Infrared Spectroscopy (FT-IR)

The obtained FTIR spectra (Figure 17) allow the examination of the evolution of some functional groups interacting in the material. FTIR analysis was conducted on powders sintered at 1100 °C. No considerable changes are observed after doping with Ga.

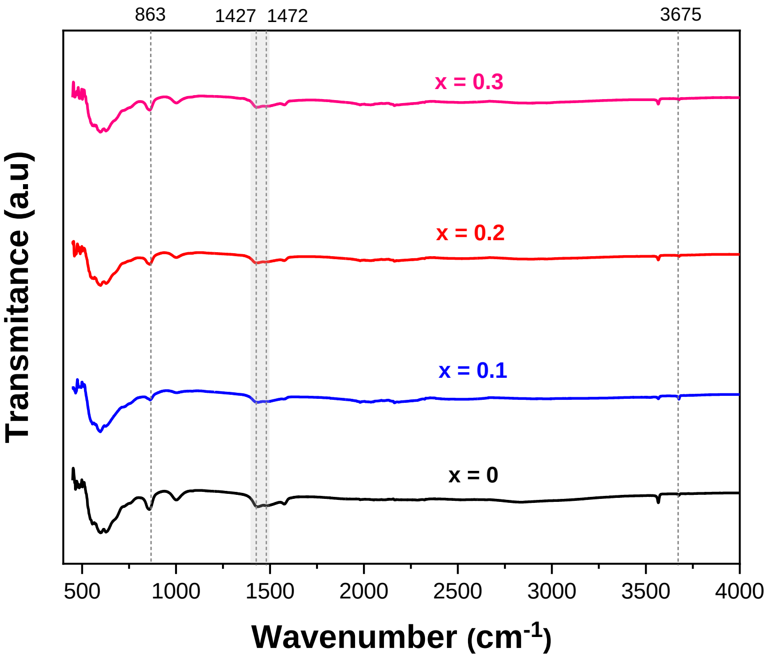

Figure 17. FTIR spectra of $Li_{7-3x}Ga_xLa_3Zr_2O_{12}$ (x = 0, 0.1, 0.2 and 0.3) samples.

The vibrational modes present between 500 and 800 cm^{-1} corresponds to metal (M) oxygen interactions (La-O, Zr-O, Ga-O) [66]. Peaks at 863, 1427 and 1472 cm^{-1}, assigned to C-O bonds, are observed in all the samples, indicating the presence of Li_2CO_3 which is typically formed on the surface of LLZO when reacting with the CO_2 [67, 68]. It is very difficult to avoid interaction with air during heating and handling processes. Similarly, a peak of lower intensity is observed at 3675 cm^{-1}, being more pronounced in x = 0 and 0.1 samples. This peak corresponds to H-O bonds formed due to the absorption of water on the pellet surface from the ambient humidity [69, 67]. The low signal intensity may be due to the dry storage where the pellets are kept most of the time in a vacuum desiccator.

6.1.4 Field Emission Scanning Electron Microscopy (FE-SEM)

Figure 18 shows FE-SEM images of the morphology of the pellets sintered at 1100 °C. All samples contain abundant pores and nonuniform "loose" grains with clear boundaries, indicating an inadequate sintering [70]. For SSB applications, high relative densities, near to 100% are needed. The subsequently measured low relative density of the pellets (Table 3) coincides with that shown in the images. In the four images there are no significant differences in their morphology, i.e., the gallium doped samples and the pure LLZO sample are similar. Therefore, the addition of Ga does not promote densification.

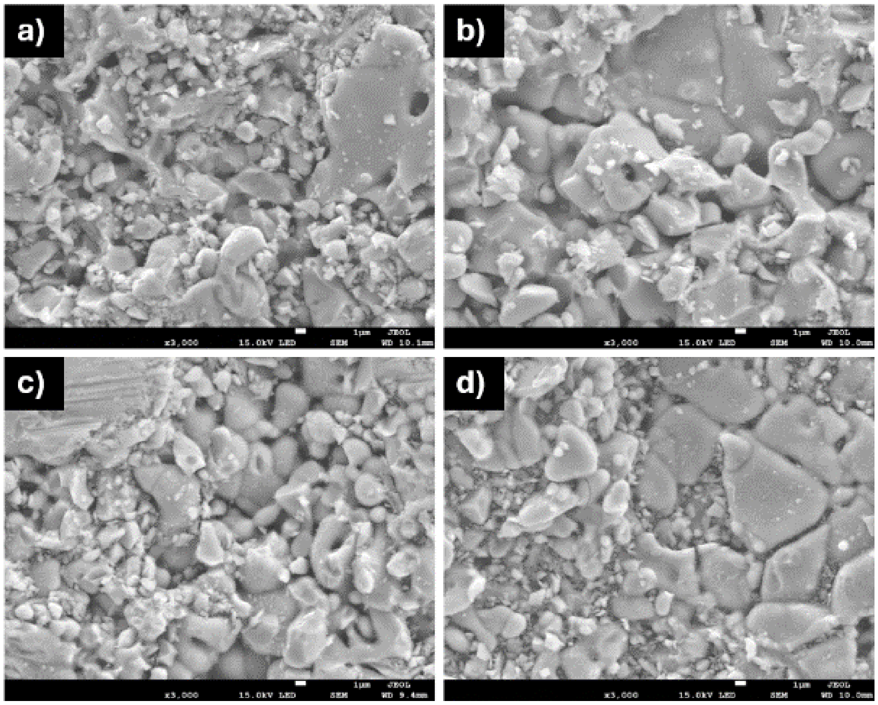

Figure 18. FE-SEM images of $Li_{7-3x}Ga_xLa_3Zr_2O_{12}$: (a) x = 0, (b) x = 0.1, (c) x = 0.2 and (d) x = 0.3; sintered at 1100 °C.

These results are consistent with those reported, where Ga-doped LLZO often experiences anomalous grain growth, resulting in loose grain boundaries and low mechanical strengths. On the other hand, Ga^{3+} competes with Li^{+} for occupying the same sites in the crystal lattice. These two phenomena often complicate the sintering of LLZO and reduce the consistency of the ceramic [71, 70].

EDS analyses were carried out to confirm the existence of Ga in the doped samples. Figure 19 shows the presence of Ga indicating its incorporation in the LLZO structure. Similarly, all images revealed the presence of La, Zr and O contents, with no significant impurities. However, a carbon signal was observed, probably attributable to the presence of Li_2CO_3 due to its interaction with the environment during storage. This result is consistent with the signals observed in the FTIR spectra.

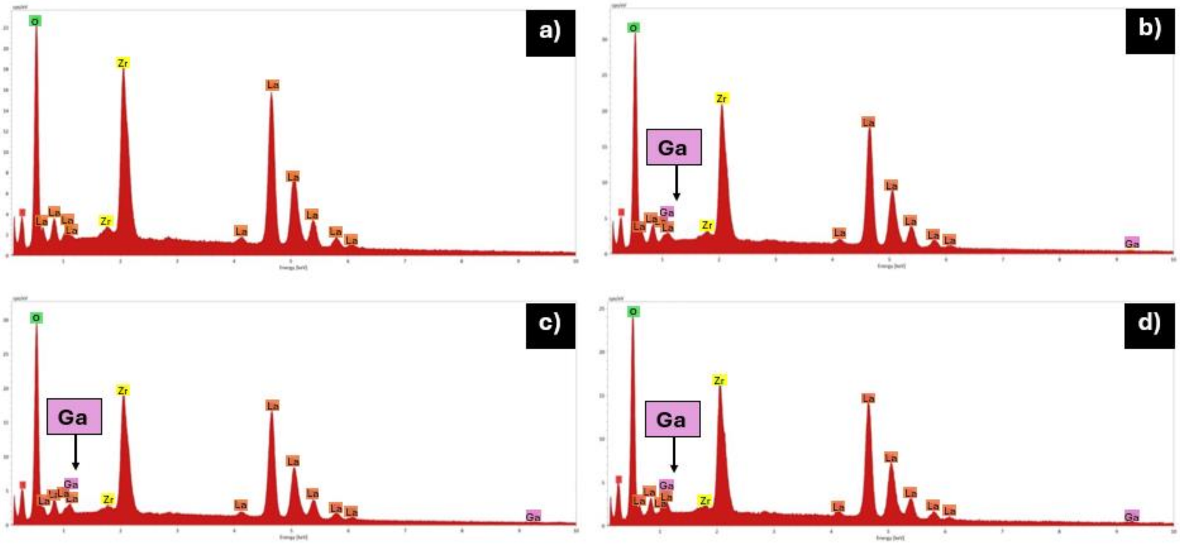

Figure 19. EDS analysis of $Li_{7-3x}Ga_xLa_3Zr_2O_{12}$ samples: (a) x = 0, (b) x = 0.1, (c) x = 0.2 and (d) x = 0.3.

6.1.5 Electrical conductivity measurement

Figure 20 illustrates the Nyquist plots and its respective fitting, obtained from impedance measurements at 25 °C, 125 °C and 200 °C, performed on the $Li_{7-3x}Ga_xLa_3Zr_2O_{12}$ (x = 0, 0.1, 0.2 and 0.3) pellets sintered at 1100 °C. The diagrams at room temperature show the presence of a single semicircle in the high frequency region, corresponding to the resistance contributions from the bulk and grain boundary; and a line in the low frequency region, associated with the resistance (lithium-ion blocking) coming from the Ag electrodes [73, 74].

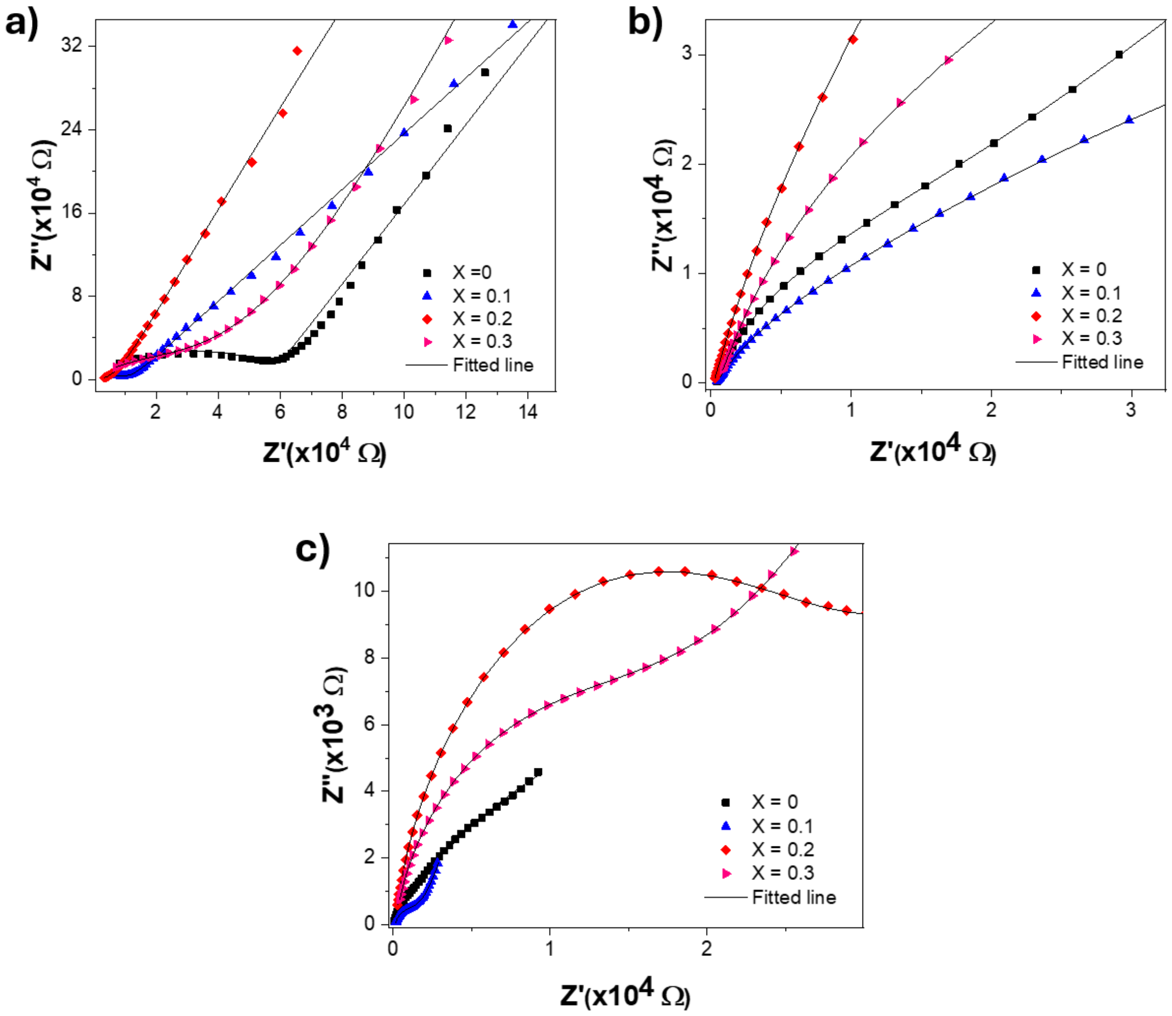

Figure 20. Nyquist plots from the $Li_{7-3x}Ga_xLa_3Zr_2O_{12}$ (x = 0, 0.1, 0.2 and 0.3) pellets sintered at 1100 °C, at: (a) 25 °C, (b) 125 °C and (c) 200 °C.

Since only a semicircle is visible in the impedance diagram, it is not possible to precisely distinguish the separate contributions from the bulk and grain boundaries. Therefore, the intersection of the semicircle at high frequencies on the real axis of the impedance (Z') represents the total resistance of the sample, and the line corresponds to the resistance of the silver electrodes used for the measurements [36]. This type of shape describes a mainly ionic conduction process [74]. In the case of the room temperature Nyquist plots (Figure 20a) it can be observed that the total resistance decreases with the increase in temperature. Similarly, the sample with x = 0.2 exhibits the lowest resistance at room temperature among all the studied compositions.

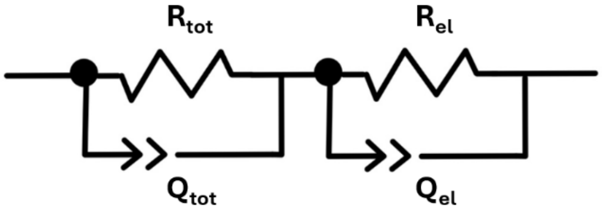

Figure 21. Equivalent circuit employed to fit the experimental data.

The fitted data represent the equivalent circuit ($(R_{tot}Q_{tot})(R_{el}Q_{el})$) describing the experimental data, where R is the resistance, Q the constant phase element, the subscript "tot" corresponds to the total resistance and the subscript "el" refers to the contribution of the electrodes.

Figure 22 presents the fits of the Arrhenius equation (equation 3) and the activation energy values obtained from the total conductivity of all samples.

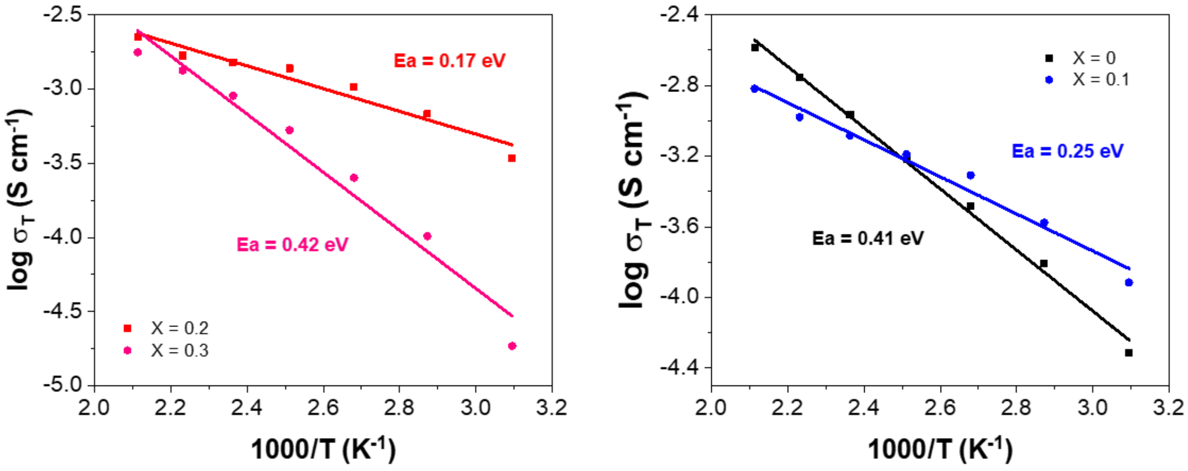

Figure 22. Arrhenius fits of the calculated conductivities for $Li_{7-3x}Ga_xLa_3Zr_2O_{12}$: (a) x = 0 and x = 0.1; (b) x = 0.2 and x = 0.3.

Table 4 shows the relative densities of the $Li_{7-3x}Ga_xLa_3Zr_2O_{12}$ (x = 0, 0.1, 0.2 and 0.3) pellets sintered at 1100 °C, the conductivity values at different temperatures and the activation energy. The relative densities were obtained by dividing the calculated density value by its theoretical density. The estimated theoretical density used for the calculations is 5.107 g cm^{-3} [73].

The point defects produced by the addition of Ga, in addition to the Coulombic repulsion between Li^+ - Ga^{3+} that causes a redistribution of Li ions in the crystal lattice, may increase the mobility of the ions and, therefore, their ionic conductivity [75, 76].

From the impedance plots, it can be clearly seen that sample doped with x = 0.2 of Ga has the lowest total resistance and therefore the highest ionic conduction. This result agrees with the calculated values, where among the Ga-doped series, $Li_{6.4}Ga_{0.2}La_3Zr_2O_{12}$ showed the lowest total resistance, and the highest total ionic conductivity in the range of 25 - 200 °C. These results agree with that reported by X. Huang *et. al* [70].

Table 4. Relative density, ionic conductivity at different temperatures, and activation energy of $Li_{7-3x}Ga_xLa_3Zr_2O_{12}$ samples sintered at 1100 °C.

Garnet	**Relative density (%)**	**Temperature (°C)**	**σ_{dc} (S cm^{-1})**	**E_a (eV)**
$Li_7La_3Zr_2O_{12}$	89.17	25	4.48×10^{-06}	0.41
		50	4.86×10^{-05}	
		75	1.56×10^{-04}	
		100	3.30×10^{-04}	
		125	6.06×10^{-04}	
		150	1.09×10^{-03}	
		175	1.77×10^{-03}	
		200	2.59×10^{-03}	
$Li_{6.7}Ga_{0.1}La_3Zr_2O_{12}$	92.74	25	2.79×10^{-05}	0.25
		50	1.21×10^{-04}	
		75	2.65×10^{-04}	
		100	4.92×10^{-04}	
		125	6.47×10^{-04}	
		150	8.26×10^{-04}	
		175	1.05×10^{-03}	
		200	1.52×10^{-03}	
$Li_{6.4}Ga_{0.2}La_3Zr_2O_{12}$	91.33	25	1.58×10^{-04}	0.17
		50	3.41×10^{-04}	
		75	6.79×10^{-04}	
		100	1.03×10^{-03}	
		125	1.38×10^{-03}	
		150	1.51×10^{-03}	
		175	1.68×10^{-03}	
		200	2.25×10^{-03}	
$Li_{6.1}Ga_{0.3}La_3Zr_2O_{12}$	92.73	25	4.50×10^{-06}	0.42
		50	1.85×10^{-05}	
		75	1.02×10^{-04}	
		100	2.53×10^{-04}	
		125	$5.2\ \times10^{-04}$	
		150	9.02×10^{-03}	
		175	1.34×10^{-03}	
		200	1.77×10^{-03}	

6.2 CO-DOPED SAMPLES

6.2.1 TGA/DSC analysis

Figure 23 shows the TGA/DSC curves of $Li_{6.1+y}Ga_{0.2}La_3Zr_{2-y}Gd_yO_{12}$ (y = 0, 0.1, 0.2, 0.3) samples from room temperature to 1100 °C in air. Powders preheated at 600 °C for 1 h were used for the analysis. All the TGA plots show three significant weight losses stages, showing a behavior comparable to that of the Ga-doped samples.

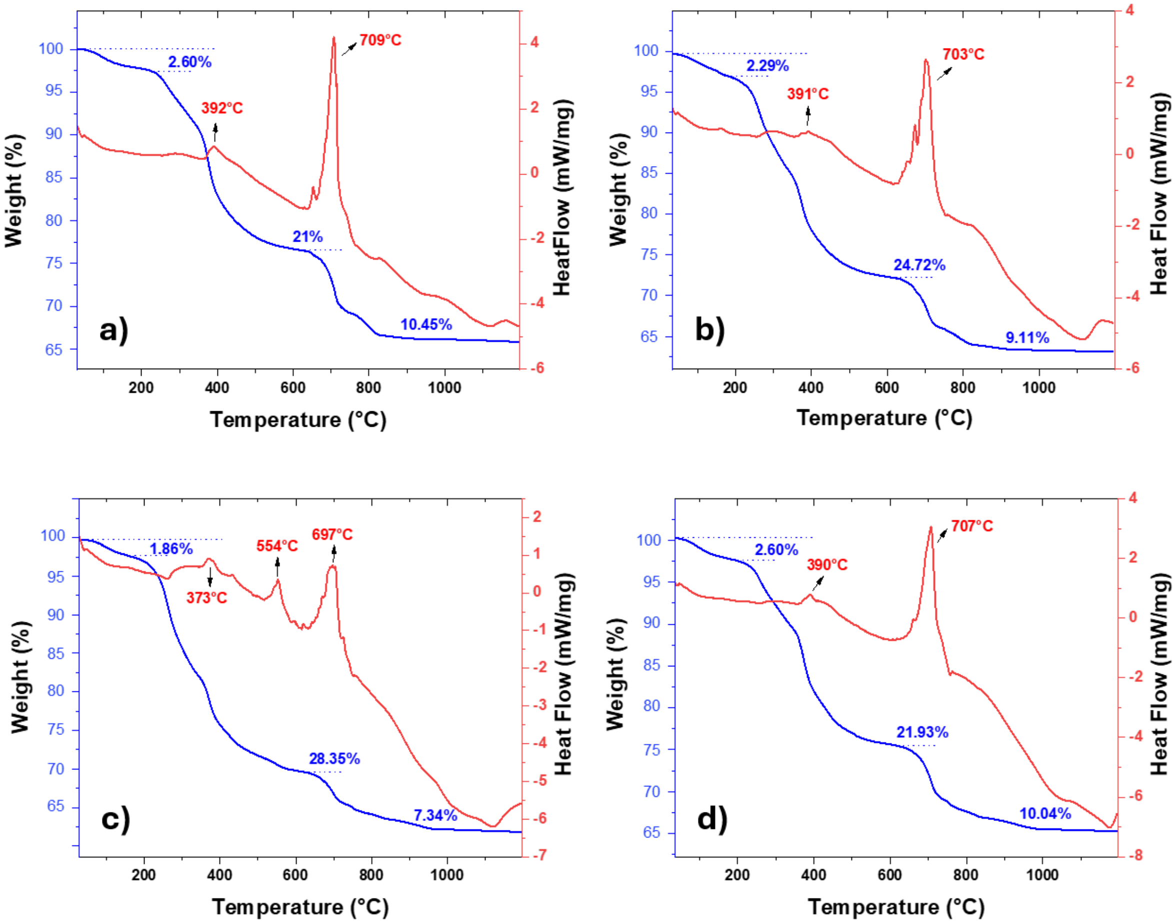

Figure 23. TGA-DSC curves for the $Li_{6.1+y}Ga_{0.2}La_3Zr_{2-y}Gd_yO_{12}$ powders preheated at 600 °C: (a) y = 0.2, (b) y = 0.4, (c) y = 0.6 and (d) y = 0.8.

The first step of weight loss occurring around 250 °C may be associated with the evaporation of hygroscopic H_2O due to the interaction between ambient humidity and the material [50]. The second stage of weight loss begins around 300 °C and ends at 600 °C and is associated with the degradation and oxidation of remaining organic residues [53]. The last stage of weight loss after 600 °C can be related with the decomposition of excess Li_2CO_3 formed by the interaction of the material with moisture and ambient, this is attributed to the prolonged storage of the samples before analysis. [77]. This interaction was described by Wang [78], by means of a reversible reaction of:

$$Li_7La_3Zr_2O_{12} + xCO_2 \leftrightarrow Li_{7-2x}La_3Zr_2O_{12-x} + xLi_2CO_3 \quad (6)$$

The TGA plots show that above 800 °C the weight loss is negligible, indicating the transformation of the precursors into oxides and consequently the formation of the LLZO structure.

All the samples show two main exothermic peaks around 390 °C and 700 °C. The small exothermic peaks at 390 °C can be attributed to degradation of the organic residuals and the intense exothermic peak that occurs before the final weight loss, around 700 °C, corresponds to the formation of the final phase of the LLZO [53].

The sample y = 0.6 has an additional exothermic peak at 554 °C that could not be identified. Furthermore, in all the DSC patterns some additional small exothermic peaks can be perceived, which may be related to the formation of secondary phases or changes in the crystalline structure within the material, which would agree with the results obtained in the XRD patterns.

6.2.2 X-ray diffraction

Figure 24 shows the diffraction patterns of the samples calcined at 875 °C and sintered at 1100 °C. In all the samples after calcination, a mainly cubic structure with a space group Ia-3d was obtained (black lines in Figure 24b, PDF - 04 - 019 - 8837). However, in the compositions of y = 0.2 and y = 0.8, coexisting t-LLZO and c-LLZO phases can be observed, in addition to some impurities.

For the y = 0.2, pure cubic phase was obtained after sintering at 1100 °C, however, for higher concentrations of Gd (y = 0.4, 0.6 and 0.8), impurities were observed.

Most of the impurities obtained in all XRD patterns could be related to the disorder in the crystal lattice of LLZO caused by the substitution of Zr^{4+} (0.72 Å), in the six-fold coordination arrangement, by Gd^{3+} (0.94 Å) which has a larger radius size. The main impurity in all samples is the presence of the $La_2Zr_2O_7$ phase, that could be formed by the decomposition in the cubic structure caused by the lattice disorder [50].

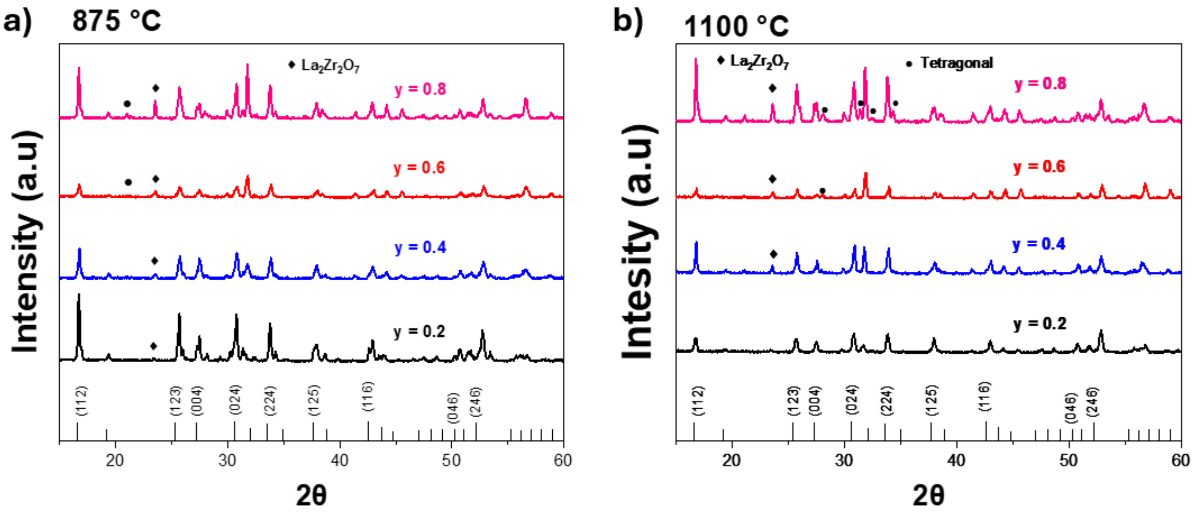

Figure 24. XRD patterns of $Li_{6.1+y}Ga_{0.2}La_3Zr_{2-y}Gd_yO_{12}$ (y = 0.2, 0.4, 0.6 and 0.8) samples calcined at (a) 875 °C and sintered at (b) 1100 °C.

The XRD results support the TGA/DSC diagrams, where the formation of secondary exothermic peaks was observed, which could be due to the formation of impurities.

6.2.3 Fourier Transform Infrared Spectroscopy (FT-IR)

Figure 25 shows the FTIR analysis performed on the co-doped powders sintered at 1100 °C. No considerable changes are observed after co-doping with Gd, presenting almost the same signals as those obtained in Ga-doped samples. The vibrational modes present between 500 and 800 cm^{-1} corresponds to metal (M) oxygen interactions (La-O, Zr-O, Ga-O, Gd-O) [66]. The peaks at 863, 1427 and 1472 cm^{-1}, assigned to C-O bonds, are observed in all samples indicating the presence of Li_2CO_3 formed on the surface of LLZO when reacting with the CO_2 [67, 68]. The signals corresponding to C-O are of higher intensity than in the Ga-doped series. This increase in the signals could be due to an increase in the amount of these functional groups in the material. Similarly, a peak of lower intensity is observed at 3675 cm^{-1}, that corresponds to H-O bonds formed due to the absorption of water on the pellet surface from the ambient humidity [69, 67].

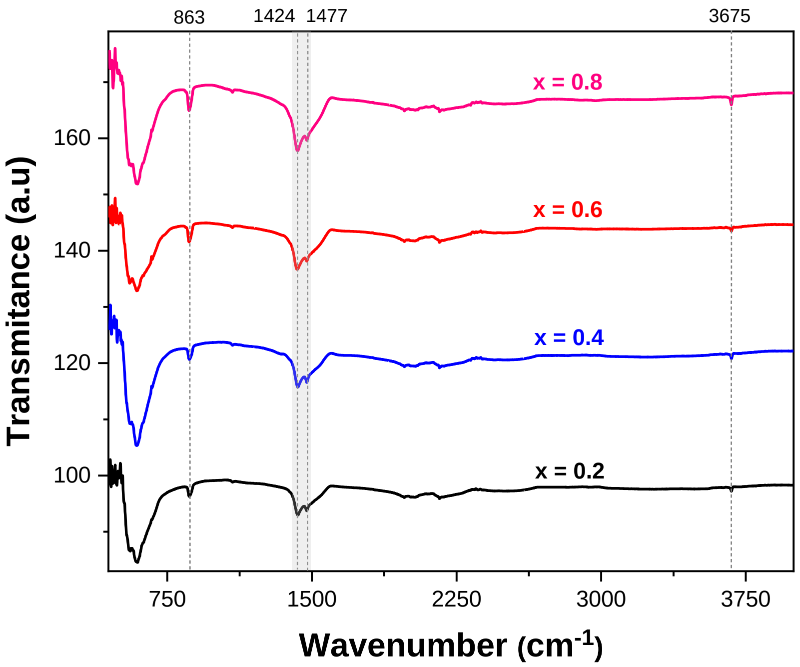

Figure 25. FTIR spectra of $Li_{6.1+y}Ga_{0.2}La_3Zr_{2-y}Gd_yO_{12}$ (y = 0.2, 0.4, 0.6 and 0.8) samples.

6.2.4. Field Emission Scanning Electron Microscopy (FE-SEM)

The FE-SEM images of the pellets sintered at 1100 °C are shown in Figure 26. Compared to the Ga samples, lower porosity and larger grains with unclear boundaries are observed, indicating an improvement in sintering. This is consistent with the high relative density obtained for the pellets (Table 5). A dense microstructure in solid electrolytes is important for SSB applications as it ensures better mechanical properties and prevents the growth of lithium dendrites and their propagation in the battery [79].

In the sample with y = 0.2, (Figure 26a) more defined grains are observed with some voids between grains, however, as the gadolinium content increases, the pores disappear, and the grains become increasingly compact. Upon reaching a composition of y = 0.8, no distinct grains are observed, and the porosity is nearly eliminated. The calculated relative densities of the samples increased as the amount of Gd increased. This, along with the observations from the micrographs, suggests that the addition of Gd promotes densification by increasing the density of the material [79].

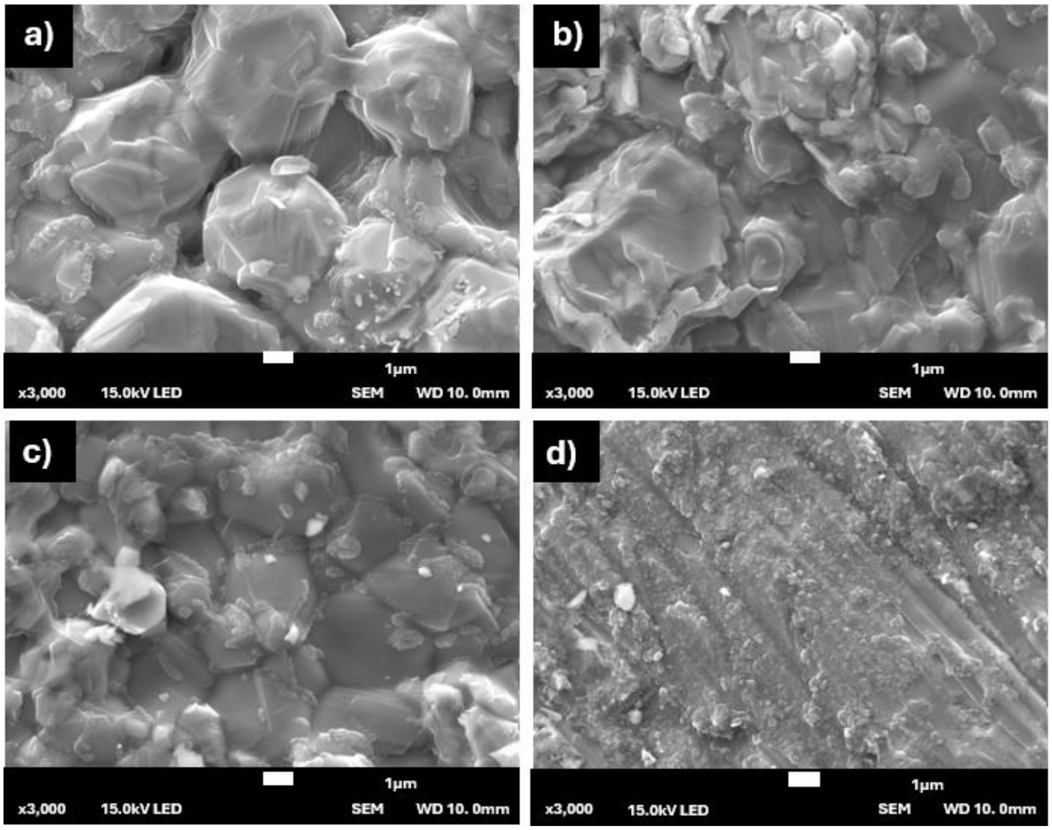

Figure 26. FE-SEM images of $Li_{6.1+y}Ga_{0.2}La_3Zr_{2-y}Gd_yO_{12}$: (a) y = 0.2, (b) y = 0.4, (c) y = 0.6 and (d) y = 0.8 sintered at 1100 °C.

EDS analyses (Figure 27) were performed to identify the elements present in the samples. All images revealed the presence of La, Zr, O, Ga and Gd confirming the incorporation of Ga and Gd in the LLZO structure. No significant impurities were detected in these spectra since the carbon signal may be due to the presence of Li_2CO_3.

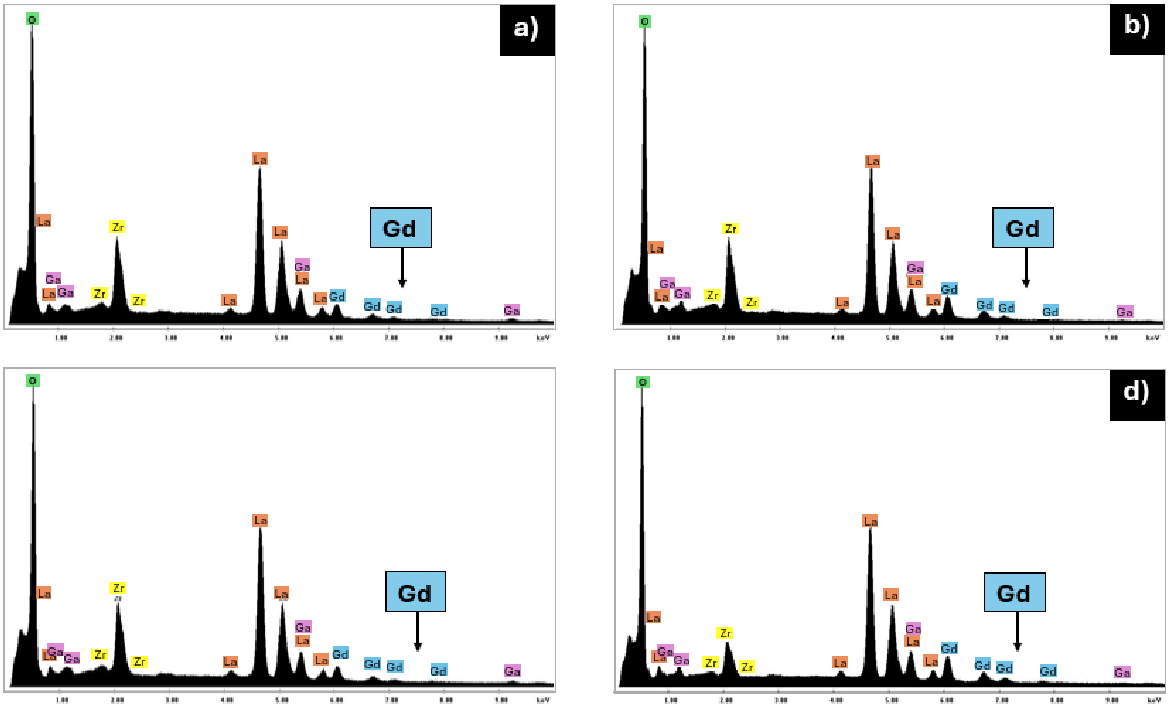

Figure 27. EDS analysis of $Li_{6.1+y}Ga_{0.2}La_3Zr_{2-y}Gd_yO_{12}$ samples: (a) y = 0.2, (b) y = 0.4, (c) y = 0.6 and (d) y = 0.8.

6.2.5 Electrical conductivity measurement

Figure 28 illustrates the Nyquist plots and its respective fitting, obtained from impedance measurements at 25 °C, 125 °C and 200 °C, performed on the $Li_{6.1+y}Ga_{0.2}La_3Zr_{2-y}Gd_yO_{12}$ (y = 0.2, 0.4, 0.6 and 0.8) pellets. In the diagrams at room temperature (Figure 28a), the semicircle in the high-frequency region, which corresponds to the bulk and grain boundary resistance contributions, is smaller than those present in the Ga-doped samples. Moreover, this contribution continues to decrease with increasing temperature.

The absence of clear semicircles supports the observations made in the micrographs, where a decrease in grain boundaries was observed with increasing amount of Gd, contributing to smaller grain boundary resistances at low temperatures [50].

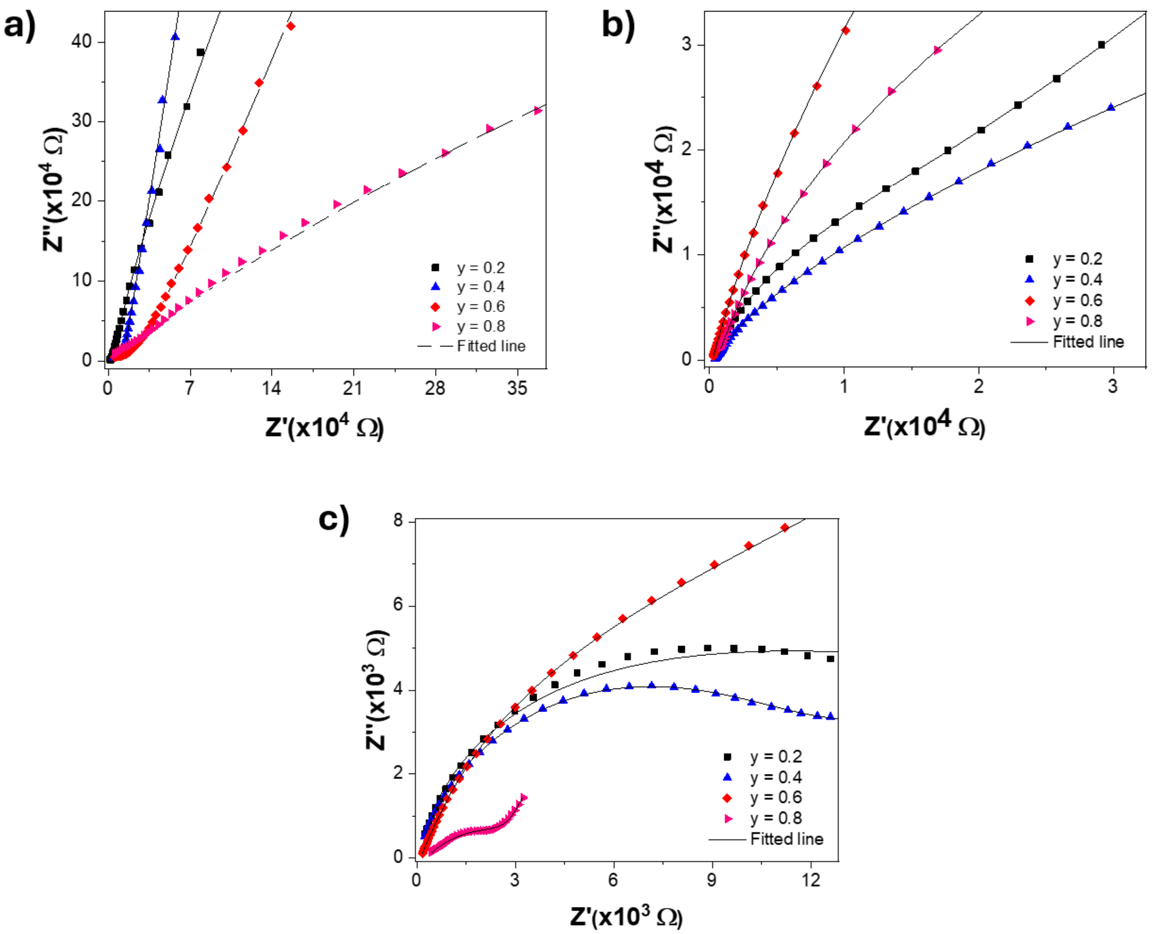

Figure 28. Nyquist plots from the $Li_{6.1+y}Ga_{0.2}La_3Zr_{2-y}Gd_yO_{12}$ (y = 0.2, 0.4, 0.6 and 0.8) pellets sintered at 1100 °C, at: (a) 25 °C, (b) 125 °C and (c) 200 °C.

The fitted data represent the equivalent circuit $(R_{tot}Q_{tot})(R_{el}Q_{el})$ describing the experimental data, where R is the resistance, Q the constant phase element, the subscript "tot" corresponds to the total ionic conductivity and the subscript "el" refers to the contribution of the electrodes. The equivalent circuit used to describe the co-doped samples results is the same as for the Ga-doped samples. The total resistance is obtained from the fitted values and the total ionic conductivity is calculated using Equation 2.

The activation energies were estimated from the correlation of the temperature with the conductivity using the Arrhenius equation (Equation 3). Figure 29 shows the fits of the Arrhenius equation applied to the total conductivity values of all the samples.

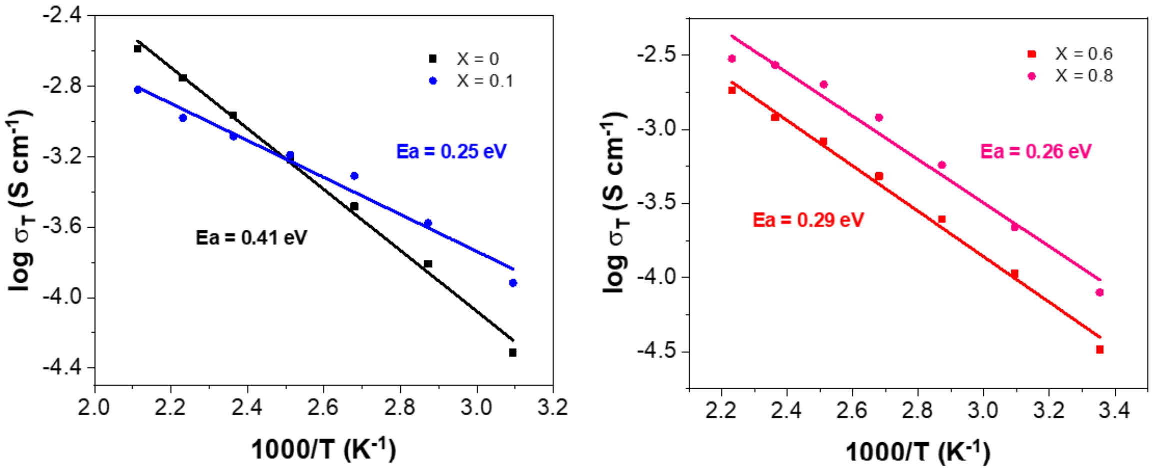

Figure 29. Arrhenius fits of the calculated conductivities for $Li_{6.1+y}Ga_{0.2}La_3Zr_{2-y}Gd_yO_{12}$: (a) y = 0.2, y = 0.4; (b) y = 0.6 and y = 0.8.

The sample doped with y = 0.2 has the lowest activation energy, the lowest total resistance and therefore the highest ionic conductivity in the 25 - 200 °C range. $Li_{6.6}Ga_{0.2}La_3Zr_{1.8}Gd_{0.2}O_{12}$ presents twice the conductivity of that obtained in the sample $Li_{6.4}Ga_{0.2}La_3Zr_2O_{12}$, which shows that the addition of the small amount of Gd at this concentration improves the ionic conductivity. In addition, it was observed that when the Gd concentration is higher than 0.2, there is a significant reduction in conductivity. This reduction may be associated with the crystal lattice distortion observed in XRD plots due to the substitution of larger ionic radius of Gd^{3+} (1.053 Å) in place of Zr^{4+} (0.84 Å), which may block the path for Li^+ conduction [50].

Table 5 shows the relative densities of the $Li_{6.1+y}Ga_{0.2}La_3Zr_{2-y}Gd_yO_{12}$ (y = 0.2, 0.4, 0.6 and 0.8) pellets sintered at 1100 °C, the conductivity values at different temperatures and the activation energy.

Table 5. Relative density, ionic conductivity at different temperatures, and activation energy of $Li_{6.1+y}Ga_{0.2}La_3Zr_{2-y}Gd_yO_{12}$ samples sintered at 1100 °C.

Garnet	Relative density (%)	Temperature (°C)	σ_{dc} (S cm^{-1})	E_a (eV)
$Li_{6.6}Ga_{0.2}La_3Zr_{1.8}Gd_{0.2}O_{12}$	94.37	25	2.31×10^{-04}	0.13
		50	4.53×10^{-04}	
		75	8.14×10^{-04}	
		100	1.29×10^{-03}	
		125	1.52×10^{-03}	
		150	1.66×10^{-03}	
		175	1.70×10^{-03}	
		200	1.43×10^{-03}	
$Li_{6.8}Ga_{0.2}La_3Zr_{1.6}Gd_{0.4}O_{12}$	98.90	25	9.94×10^{-05}	0.27
		50	1.33×10^{-04}	
		75	3.58×10^{-04}	
		100	1.26×10^{-03}	
		125	1.93×10^{-03}	
		150	2.57×10^{-03}	
		175	2.99×10^{-03}	
		200	3.01×10^{-03}	
$Li_7Ga_{0.2}La_3Zr_{1.4}Gd_{0.6}O_{12}$	99.49	25	3.26×10^{-05}	0.29
		50	1.06×10^{-04}	
		75	2.49×10^{-04}	
		100	4.83×10^{-04}	
		125	8.31×10^{-04}	
		150	1.20×10^{-03}	
		175	1.83×10^{-03}	
		200	2.58×10^{-03}	
$Li_{7.2}Ga_{0.2}La_3Zr_{1.2}Gd_{0.8}O_{12}$	99.87	25	7.92×10^{-05}	0.26
		50	2.18×10^{-04}	
		75	5.75×10^{-04}	
		100	1.20×10^{-03}	
		125	2.01×10^{-03}	
		150	2.71×10^{-03}	
		175	3.00×10^{-03}	
		200	3.13×10^{-03}	

Finally, a comparison of the conductivity values of the best material from both doped and co-doped series and LLZO is shown on Table 6. Table shows among the different series studied $Li_{6.6}Ga_{0.2}La_3Zr_{1.8}Gd_{0.2}O_{12}$ sample exhibited the highest conductivity of 2.31×10^{-4} S cm^{-1} and the lowest activation energy of 0.13 eV.

Table 6. Comparison of relative density, ionic conductivity and activation energy of doped and co-doped samples with the best results versus pure LLZO.

Garnet	**Relative density (%)**	**Temperature (°C)**	**σ_{dc} (S cm^{-1})**	**E_a (eV)**
$Li_7La_3Zr_2O_{12}$	89.17	25	4.48×10^{-06}	0.41
		125	6.06×10^{-04}	
		200	2.59×0^{-03}	
$Li_{6.4}Ga_{0.2}La_3Zr_2O_{12}$	91.33	25	1.58×10^{-04}	0.17
		125	1.38×10^{-03}	
		200	2.25×10^{-03}	
$Li_{6.6}Ga_{0.2}La_3Zr_{1.8}Gd_{0.2}O_{12}$	94.37	25	2.31×10^{-04}	0.13
		125	1.52×10^{-03}	
		200	1.43×10^{-03}	

7. CONCLUSIONS

The doped $Li_{7-3x}Ga_xLa_3Zr_2O_{12}$ (x = 0, 0.1, 0.2, 0.3) and co-doped $Li_{6.1+y}Ga_{0.2}La_3Zr_{2-y}Gd_yO_{12}$ (y = 0.2, 0.4, 0.6 and 0.8) garnet structured oxides were synthesized successfully by the Pechini method.

In the Ga-doped samples with x = 0 and 0.1, the cubic phase was only obtained after sintering at 1100 °C. In contrast, for x = 0.2 and 0.3, the cubic structure was achieved after calcination at 875 °C. This demonstrates that the addition of Ga contributes to stabilizing the c-LLZO structure at low temperature.

Additionally, the Ga-doped pellets show a relatively low density and a microstructure containing abundant pores and non-uniform loose grains with clear boundaries, indicating inadequate sintering. Therefore, it can be concluded that the addition of Ga does not favor densification.

Among the Ga-doped series, $Li_{6.4}Ga_{0.2}La_3Zr_2O_{12}$ exhibited the lowest total resistance, and the highest ionic conductivity in the range 25 – 200 °C, obtaining a total conductivity of 1.58×10^{-04} S cm^{-1} at room temperature.

For the co-doped samples, only y = 0.2 shows a pure cubic phase after sintering at 1100 °C. For higher concentrations of Gd (y = 0.4, 0.6 and 0.8), garnet structure formed with impurities possibly related to disorder in the crystal lattice of LLZO. This disorder is likely due to the ionic size difference between Gd^{3+} and Zr^{4+}, and affects the total conductivity, being reduced with the increasing the amount of Gd. However, it was observed that the addition of Gd improves the densification of the pellets, obtaining higher relative densities of 99.87% for Gd = 0.8.

The co-doped sample $Li_{6.6}Ga_{0.2}La_3Zr_{1.8}Gd_{0.2}O_{12}$ showed the highest ionic conductivity in the 25 - 200 °C range, obtaining a total conductivity of 2.31×10^{-04} S cm^{-1} at room temperature, which is twice the value of $Li_{6.4}Ga_{0.2}La_3Zr_2O_{12}$ sample. Therefore, it can be concluded that the doping of smaller amounts ($y \leq 0.2$) of Gd improves ionic conduction by obtaining a highly densified material, for possible application as solid electrolytes in SSLIBs.

As for Gd doping and the effect on the crystal structure of LLZO, further studies are needed to determine how the addition of this element accurately distorts the ion arrangement and its ultimate effect on ionic conduction.

8. REFERENCES

[1] D. Deng. Li-ion batteries: basics, progress, and challenges. Energy Sci. Eng. 3 (2015) 385-418.

[2] M. A. U. Din, C. Li, L. Zhang, C. Han, B. Li. Recent progress and challenges on the bismuthbased anode for sodium-ion batteries and potassium-ion batteries. Mater. Today Phys. 21 (2021) 100486.

[3] A. Banerjee, X. Wang, C. Fang, E. A. Wu, Y. S. Meng. Interfaces and interphases in all-solidstate batteries with inorganic solid electrolytes. Chem. Rev. 120 (2020) 6878-6933.

[4] A. Yoshino. The birth of the lithium-ion battery. Angew. Chem. Int. Ed. 51 (2012) 5798-5800.

[5] W. Xia, Y. Zhao, F. Zhao, K. Adair, R. Zhao, S. Li, R. Zou, Y. Zhao, X. Sun. Antiperovskite electrolytes for solid-state batteries. Chem. Rev. 122 (2022) 3763-3819.

[6] Q. Liu, Z. Cheng, C. Han, Y. Fu, S. Li, Y. He, F. Kang, B. Li. Challenges and perspectives of garnet solid electrolytes for all solid-state lithium batteries. J. Power Sources. 389 (2018): 120-134.

[7] J. Wen, D. Zhao, C. Zhang. An overview of electricity powered vehicles: Lithium-ion battery energy storage density and energy conversion efficiency. Renew. Energy. 162 (2020) 1629-1648.

[8] J. Li, Z. Liu, W. Ma, H. Dong, K. Zhang, R. Wang. Low-temperature synthesis of cubic phase $Li_7La_3Zr_2O_{12}$ via sol-gel and ball milling induced phase transition. J. Power Sources. 412 (2019) 189-196.

[9] X. Huang, T. Xiu, M. E. Badding, Z. Wen. Two-step sintering strategy to prepare dense Li-Garnet electrolyte ceramics with high Li+ conductivity. Ceram. Int. 44 (2018) 5660-5667.

[10] T. Zhang, Y. Liu, T. D. Christopher, S. Huang, T. Sohel, X. Song, W. Gao, P. Cao. The effect of water vapor on structure and electrochemical performance of an aluminum-free niobium-doped garnet electrolyte. Ceram. Int. 46 (2020) 3889-3895.

[11] L. Shen, L. Wang, Z. Wang, C. Jing, L. Peng, X. Pang, J. Sung, R. Yang. Preparation and characterization of Ga and Sr co-doped $Li_7La_3Zr_2O_{12}$ garnet-type solid electrolyte. Solid State Ion. 339 (2019) 114992.

[12] O. Sharifi, M. Golmohammad, M. Soozandeh, A. S. Mehranjani. Improved Ga-doped $Li_7La_3Zr_2O_{12}$ garnet-type solid electrolytes for solid-state Li-ion batteries. J. Solid State Electrochem. (2023) 1-12.

[13] I. Dincer. Environmental impacts of energy. Energy policy. 27 (1999) 845-854. [12] D. Larcher, J. M. Tarascon. Towards greener and more sustainable batteries for electrical energy storage. Nat. Chem. 7 (2015) 19-29

[14] Y. Yang, E. G. Okonkwo, G. Huang, S. Xu, W. Sun, Y. He. On the sustainability of lithium ion battery industry–A review and perspective. Energy Storage Mater. 36 (2021) 186-212.

[15] D. Larcher, J. M. Tarascon. Towards greener and more sustainable batteries for electrical energy storage. Nat. Chem. 7 (2015) 19-29.

[16] B. E. Murdock, K. E. Toghill, N. Tapia-Ruiz. A perspective on the sustainability of cathode materials used in lithium-ion batteries. Adv. Energy Mater. 11 (2021) 2102028.

[17] R. R. Kumar, K. Alok. Adoption of electric vehicle: A literature review and prospects for sustainability. J. Clean. Prod. 253 (2020) 119911.

[18] C. Iclodean, B. Varga, N. Burnete, D. Cimerdean, B. Jurchis. Comparison of different battery types for electric vehicles. IOP Conf. Ser.: Mater. Sci. Eng. 252 (2017) 012058.

[19] H. Zou, E. Gratz, D. Apelian, Y. Wang. A novel method to recycle mixed cathode materials for lithium ion batteries. Green Chem. 15 (2013) 1183-1191.

[20] B. Kennedy, D. Patterson, S. Camilleri. Use of lithium-ion batteries in electric vehicles. J. Power Sources. 90 (2000) 156-162.

[21] X. Shen, H. Liu, X. B. Cheng, C. Yan, J. Q. Huang. Beyond lithium ion batteries: Higher energy density battery systems based on lithium metal anodes. Energy Storage Mater. 12 (2018) 161-175.

[22] X. Fu, D. Yu, J. Zhou, S. Li, X. Gao, Y. Han, P. Qi, X. Feng. Inorganic and organic hybrid solid electrolytes for lithium-ion batteries. CrystEngComm. 18 (2016) 4236-4258.

[23] L. Han, M. L. Lehmann, J. Zhu, T. Liu, Z. Zhou, X. Tang, C. T. Heish, A. P. Sokolov, P. Cao, X. C. Chen, T. Saito. Recent developments and challenges in hybrid solid electrolytes for lithiumion batteries. Front. Energy Res. 8 (2020) 202.

[24] C. Cao, Z. B. Li, X. L. Wang, X. B. Zhao, W. Q. Han. Recent advances in inorganic solid electrolytes for lithium batteries. Front. Energy Res. 2 (2014) 25

[25] Z. J. Zhang, P. Ramadass, W. Fang. Lithium-ion batteries Advances and Applications, Elsevier, 2014, pp. 409-435.

[26] [19] X. Ke, Y. Wang, G. Ren, C. Yuan. Towards rational mechanical design of inorganic solid electrolytes for all-solid-state lithium-ion batteries. Energy Stor. Mater. 26 (2020) 313-324.

[27] F. Zheng, M. Kotobuki, S. Song, M. O. Lai, L. Lu. Review on solid electrolytes for all-solidstate lithium-ion batteries. J. Power Sources. 389 (2018) 198-213.

[28] R. Hausbrand, G. Cherkashinin, H. Ehrenberg, M. Groting, K. Able, C. Hess, W. Jaegermann. Fundamental degradation mechanisms of layered oxide Li-ion battery cathode materials: Methodology, insights and novel approaches. Mater. Sci. Eng.: B. 192 (2015) 3-25.

[29] J. Schnell, T. Günther, T. Knoche, C. Vieider, L. Köhler, A. Just, M. Keller, S. Passerini, G. Reinhart. All-solid-state lithium-ion and lithium metal batteries–paving the way to large-scale production. J. Power Sources. 382 (2018) 160-175.

[30] P. M. Gonzalez Puente, S. Song, S. Cao, L. Z. Rannalter, Z. Pan, X. Xiang, Q. Shen, F. Chen. Garnet-type solid electrolyte: Advances of ionic transport performance and its application in allsolid-state batteries. J. Adv. Ceram. (2021) 1-40. 22

[31] A. Kim, S. Woo, M. Kang, H. Park, B. Kang. Research progresses of garnet-type solid electrolytes for developing all-solid-state Li batteries. Front. Chem. 8 (2020) 468.

[32] R. Chen, Q. Li, X. Yu, L. Chen, H. Li. Approaching practically accessible solid-state batteries: stability issues related to solid electrolytes and interfaces. Chem. Rev. 120 (2019) 6820-6877.

[33] E. Umeshbabu, B. Zheng, Y. Yang. Recent progress in all-solid-state Lithium− Sulfur batteries using high Li-ion conductive solid electrolytes. Electrochem. Energy Rev. 2 (2019) 199-230.

[34] K. Takada. Progress in solid electrolytes toward realizing solid-state lithium batteries. J. Power Sources. 394 (2018) 74-85.

[35] M. M. Raju, F. Altayran, M. Jhonson, D. Wang, Q. Zhang. Crystal structure and preparation of $Li_7La_3Zr_2O_{12}$ (LLZO) solid-state electrolyte and doping impacts on the conductivity: An overview. Electrochem. 2 (2021) 390-414.

[36] J. F. Wu, E. Y. Chen, Y. Yu, L. Liu, Y. Wu, W. K. Pang, V. K. Peterson, X. Guo. Gallium-doped $Li_7La_3Zr_2O_{12}$ garnet-type electrolytes with high lithium-ion conductivity. ACS appl. Mater. Interfaces. 9 (2017) 1542-1552.

[37] X. Xiang, Y. Liu, F. Chen, W. Yang, J. Yang, X. Ma, D. Cheng, K. Su, Q. Shen, L. Zhang. Crystal structure and lithium ionic transport behavior of Li site doped $Li_7La_3Zr_2O_{12}$. J. Eur. Ceram. Soc. 40 (2020) 3065-3071.

[38] J. Awaka, N. Kijima, H. Hayakawa, J. Akimoto. Synthesis and structure analysis of tetragonal $Li_7La_3Zr_2O_{12}$ with the garnet-related type structure. J. Solid State Chem. 182 (2009) 2046-2052.

[39] J. Awaka, A. Takashima, K. Kataoka, N. Kijima, Y. Idemoto, J. Akimoto. Crystal structure of fast lithium-ion-conducting cubic $Li_7La_3Zr_2O_{12}$. Chem. Lett. 40 (2011) 60-62.

[40] M. Xu, M. S. Park, J. M. Lee, T. Y. Kim, Y. S. Park, E. Ma. Mechanisms of Li+ transport in garnet-type cubic $Li_{3+x}La_3M_2O_{12}$ (M= Te, Nb, Zr). Phys. Rev. B. Condens. Matter Mater. Phys. 85 (2012) 052301.

[41] C. Wang, K. Fu, S. P. Kammampata, D. W. McOwen, A. J. Samson, L. Zhang, G. T. Hitz, A. M. Nolan, E. D. Wachsman, Y. Mo, V. Thangadurai, L. Hu. Garnet-type solid-state electrolytes: materials, interfaces, and batteries. Chem. Rev. 120 (2020) 4257-4300.

[42] B. Zhang, R. Tan, L. Yang, J. Zheng, K. Zhang, S. Mo, S. Z. Lin, F. Pan. Mechanisms and properties of ion-transport in inorganic solid electrolytes. Energy Storage Mater. 10 (2018): 139-159.

[43] A. K. Baral, S. Narayanan, F. Ramezanipour, V. Thangadurai. Evaluation of fundamental transport properties of Li-excess garnet-type $Li_{5+2x}La_3Ta_{2-x}Y_xO_{12}$ (x= 0.25, 0.5 and 0.75) electrolytes using AC impedance and dielectric spectroscopy. Phys. Chem. Chem. Phys. 16 (2014) 11356-11365.

[44] Y. Luo, X. Li, Y. Zhang, L. Ge, H. Chen, L. Guo. Electrochemical properties and structural stability of Ga-and Y-co-doping in $Li_7La_3Zr_2O_{12}$ ceramic electrolytes for lithium-ion batteries. Electrochim. Acta. 294 (2019) 217-225.

[45] E. Enkhbayar, J. Kim. Study of Codoping Effects of Ta^{5+} and Ga^{3+} on Garnet $Li_7La_3Zr_2O_{12}$. ACS omega. 7 (2022) 47265-47273.

[46] Z. Cao, X. Cao, X. Liu, W. He, Y. Gao, J. Liu, J. Zheng. Effect of Sb-Ba codoping on the ionic conductivity of $Li_7La_3Zr_2O_{12}$ ceramic. Ceram. Int. 41 (2015) 6232-6236

[47] L. Zhang, Q. Zhuang, R. Zheng, Z. Wang, H. Sun, H. Arandiyan, Y. Wang, Y. Liu, Z. Shao. Recent advances of $Li_7La_3Zr_2O_{12}$-based solid-state lithium batteries towards high energy density. Energy Storage Mater. 49 (2022) 299-338.

[48] J. F. Wu, W. K. Pang, V. K. Peterson, L. Wei, X. Guo. Garnet-type fast Li-ion conductors with high ionic conductivities for all-solid-state batteries. ACS Appl. Mater. Interfaces. 9 (2017) 12461-12468.

[49] E. Il'ina. Recent Strategies for Lithium-Ion Conductivity Improvement in $Li_7La_3Zr_2O_{12}$ Solid Electrolytes. Int. J. Mol. Sci. 24 (2023) 12905.

[50] S. Song, B. Chen, Y. Ruan, J. Sun, L. Yu, Y. Wang, J. Thokchom. Gd-doped $Li_7La_3Zr_2O_{12}$ garnet-type solid electrolytes for all-solid-state Li-Ion batteries. Electrochim. Acta. 270 (2018) 501-508.

[51] Y. Luo, Y. Zhang, Q. Zhang, Y. Zheng, H. Chen, L. Guo. Effect of dual doping on the structure and performance of garnet-type $Li_7La_3Zr_2O_{12}$ ceramic electrolytes for solid-state lithium-ion batteries. Ceram. Int. 45 (2019)17874-17883.

[52] Y. Jin, P. J. McGinn. Al-doped $Li_7La_3Zr_2O_{12}$ synthesized by a polymerized complex method. J. Power Sources. 196 (2011) 8683-8687.

[53] I. Kokal, M. Somer, P. H. L. Notten, H. T. Hintzen. Sol–gel synthesis and lithium-ion conductivity of $Li_7La_3Zr_2O_{12}$ with garnet-related type structure. Solid State Ion. 185 (2011) 42-46.

[54] M. Kakihana, M. Yoshimura. Synthesis and characteristics of complex multicomponent oxides prepared by polymer complex method. BCSJ. 72 (1999) 1427-1443.

[55] A. E. Danks, S. R. Hall, Z. J. M. H. Schnepp. The evolution of 'sol–gel'chemistry as a technique for materials synthesis. Mater. Horiz. 3 (2016) 91-112.

[56] D. D. Athayde, D. F. Souza, A. M. A. Silva, D. Vasconcelos, E. H. M. Nunes, J. C. D da costa, W. L. Vasconcelos. Review of perovskite ceramic synthesis and membrane preparation methods. Ceram. Int. 42 (2016) 6555-6571.

[57] L. Dimesso. Pechini processes: an alternate approach of the sol–gel method, preparation, properties, and applications. Handbook of Sol-Gel Science and Technology. 2 (2016) 1-22.

[58] X. Hu, C. Shi, X. Liu, J. Zhang, G. De Schutter. A review on microstructural characterization of cement-based materials by AC impedance spectroscopy. Cem. Concr. Compos. 100 (2019) 1-14.

[59] D. C. Sinclair. Characterisation of electro-materials using ac impedance spectroscopy. Bol. Soc. Esp. Cerám. Vidr. 34.2 (1995) 55-65.

[60] A. C. Lazanas, M. I. Prodromidis. Electrochemical impedance spectroscopy─ a tutorial. ACS Meas. Sci. Au. 3.3 (2023) 162-193.

[61] J. R. Macdonald. Impedance spectroscopy and its use in analyzing the steady-state AC response of solid and liquid electrolytes. J. Electroanal. Chem. Interf. Electrochem. 223 (1987) 25-50.

[62] H. S. Magar, R. Y. Hassan, A. Mulchandani. Electrochemical impedance spectroscopy (EIS): Principles, construction, and biosensing applications. Sens. 21 (2021) 6578.

[63] S. Ohta, T. Kobayashi, T. Asaoka. High lithium ionic conductivity in the garnet-type oxide $Li_{7-X}La_3(Zr_{2-X}, Nb_X)O_{12}$ (X= 0–2). J. Power Sources. 196 (2011) 3342-3345.

[64] E. Enkhbayar, J. H. Kim. Study of codoping effects of Ta^{5+} and Ga^{3+} on garnet $Li_7La_3Zr_2O_{12}$. ACS omega. 50 (2022) 47265-47273.

[65] T. Thompson. Tetragonal vs. cubic phase stability in Al–free Ta doped $Li_7La_3Zr_2O_{12}$ (LLZO). J. Mater. Chem. A. 2 (2014) 13431-13436.

[66] K. Aravinth, P. Ramasamy, S. Sen, R. Arumugam. Tunable photoluminescence properties of Dy^{3+} doped LLZO phosphors for WLED and dosimetry applications. Ceram. Int. 48 (2022) 1402-1407.

[67] Z. F.Yow, Y. L. Oh, W. Gu, R. P. Rao, S. Adams. Effect of Li+/H+ exchange in water treated Ta-doped $Li_7La_3Zr_2O_{12}$. Solid State Ion. 292 (2016) 122-129.

[68] S. Saran, Y. R. Eker. Synthesis, structural and conductive properties of Nd doped garnet-type $Li_7La_3Zr_2O_{12}$ Li-ion conductor. Curr. Appl. Phys. 41 (2022) 1-6.

[69] Z. Zhang, L. Zhang, Y. Liu, H. Wang, C. Yu, H. Zeng, L. Wang, B. Xu. Interface-Engineered $Li_7La_3Zr_2O_{12}$-Based Garnet Solid Electrolytes with Suppressed Li-Dendrite Formation and Enhanced Electrochemical Performance. ChemSusChem. 11 (2018) 3774-3782.

[70] X. Huang, J. Su, Z. Song, T. Xiu, J. Jin, M. E. Badding, Z. Wen. Synthesis of Ga-doped $Li_7La_3Zr_2O_{12}$ solid electrolyte with high Li+ ion conductivity. Ceram. Int. 47 (2021) 2123-2130.

[71] J. Su, X. Huang, Z. Song, T. Xiu, M. E. Badding, J. Jin, Z. Wen. Overcoming the abnormal grain growth in Ga-doped $Li_7La_3Zr_2O_{12}$ to enhance the electrochemical stability against Li metal. Ceram. Int. 45 (2019) 14991-14996.

[72] W. Xia, B. Xu, H. Duan, Y. Guo, H. Kang, H. Li, H. Liu. Ionic conductivity and air stability of Al-doped $Li_7La_3Zr_2O_{12}$ sintered in alumina and Pt crucibles. ACS appl. Mater. Interfaces. 8 (2016) 5335-5342.

[73] P. Wakudkar, A. V. Deshpande. Enhancement of ionic conductivity by addition of $LiAlO_2$ in $Li_{6.6}La_3Zr_{1.6}Sb_{0.4}O_{12}$ for lithium ion battery. Solid State Ion. 345 (2020) 115185.

[74] M. Aote, A. V. Deshpande. Enhancement in Li-ion conductivity through Co-doping of Ge and Ta in garnet $Li_7La_3Zr_2O_{12}$ solid electrolyte. Ceram. Int. 49 (2023) 40011-40018.

[75] N. Birkner, C. Li, S. L. Estes, K. S. Brinkman. Gallium-Doping Effects on Structure, Lithium-Conduction, and Thermochemical Stability of $Li_{7-3x}Ga_xLa_3Zr_2O_{12}$ Garnet-Type Electrolytes. ChemSusChem. 14 (2021) 2621-2630.

[76] C. Chen, Y. Sun, L. He, M. Kotobuki, E. Hanc, Y. Chen, K. Zeng, L. Lu. Microstructural and electrochemical properties of Al-and Ga-doped $Li_7La_3Zr_2O_{12}$ garnet solid electrolytes. ACS Appl. Energy Mater. 3 (2020) 4708-4719.

[77] Y. Wang, W. Lai. Phase transition in lithium garnet oxide ionic conductors $Li_7La_3Zr_2O_{12}$: The role of Ta substitution and H2O/CO2 exposure. J. Power Sources. 275 (2015) 612-620.

[78] J. Li, Z. Liu, W. Ma, H. Dong, K. Zhang, R. Wang. Low-temperature synthesis of cubic phase $Li_7La_3Zr_2O_{12}$ via sol-gel and ball milling induced phase transition. J. Power Sources. 412 (2019) 189-196.

[79] Y. Luo, Y. Zhang, Q. Zhang, Y. Zheng, H. Chen, L. Guo. Effect of dual doping on the structure and performance of garnet-type $Li_7La_3Zr_2O_{12}$ ceramic electrolytes for solid-state lithium-ion batteries. Ceramics International 45 (2019) 17874-17883.